Demonstration of Deployment Accuracy of the Starshade Inner Disk Subsystem

Manan Arya, David Webb, John Steeves,
P. Doug Lisman, Phil Willems, S. Case Bradford,
Jet Propulsion Laboratory, California Institute of Technology, Pasadena CA

Eric Kelso, Kenzo Neff, Neal Beidleman, J. David Stienmier, Gregg Freebury,
Tendeg, Louisville CO

Andrew Tomchek, Tayler Thomas, Craig Hazelton, Kassi Butler,
Kamron Medina, Mike Pulford, Larry Adams, David Hepper, and Dana Turse
Roccor, Longmont CO

We present experimental results that demonstrate the required in-plane deployment accuracy of the starshade Inner Disk Subsystem (IDS). This effort was to address Milestone 7C of the Starshade Technology Activity S5, which requires that the in-plane deployment accuracy of the petal interfaces on the IDS be within $\pm 300\,\mu m$.

A full-scale $10\,m$-diameter IDS prototype was constructed. This prototype comprised a medium-fidelity perimeter truss, medium-fidelity spokes, and a low-fidelity optical shield (OS). The testbed also included gravity compensation systems and a laser tracker metrology system. The post-processed measurement uncertainties of the laser tracker were less than $30\,\mu m$ at the 3σ level. Design, engineering and fabrication of these components was done by JPL, Tendeg, and Roccor. Testing was performed at the Tendeg facility in Louisville, Colorado.

The IDS prototype was deployed 22 times and the locations of petal interfaces on the IDS were measured after each deployment. Based on this data, tolerance intervals were calculated that would contain 99.73% of future deployment accuracy errors with 90% confidence. These tolerance intervals are conservative estimates for 3σ bounds. The tolerance intervals for the three pertinent error components were found to be within the required allocations, with at least 19% margin.

I. Introduction

The direct imaging of exoplanets is key to their study. Directly sampling the reflected starlight from an exoplanet allows for the spectroscopic characterization of the exoplanet's atmosphere, which could provide clues about bio-signatures and habitability. However, such direct sampling is challenging given the extreme difference in the magnitude of light from the exoplanet relative to the light emitted by its host star. Starlight suppression – the reduction of the relative brightness of the host star as compared to the exoplanet – is therefore critical.

Starshades are a promising mechanism for starlight suppression.[1–3] A starshade is a screen, external to and separate from the telescope, that blocks starlight before it enters the telescope. The shape of the starshade is designed to redirect diffracted starlight away from the telescope aperture and to achieve the contrast necessary for the direct imaging of exoplanets.

The key mechanical challenges to realizing starshades are due to two properties that a starshade must have: one, the starshade diameter must be on the order of tens of meters to shade meter-scale space-based telescope apertures, whereas the largest rocket fairings are only about 5 m in diameter; and two, to achieve the desired levels of starlight suppression, the deployed in-plane shape of a starshade must be accurate to within hundreds of microns. As such, starshades must be folded to fit inside a rocket fairing for launch, and then unfolded to an accurate shape in space.

I.A. Background

NASA's Exoplanet Exploration Program (ExEP) has an activity called S5 to bring starshade technology to Technology Readiness Level 5 (TRL5).[4] This activity seeks to demonstrate advancement to TRL5 by meeting a number of milestones spread across three technology areas: one, optical testing and modeling of starlight suppression; two, formation flying between a space telescope and a starshade; and three, the design of a deployable mechanical system that is stable and accurate to the required levels.

Activities are underway to address these milestones, and a number of the milestones have already been met.[5–7] This report will address Milestone 7C, which is related to the mechanical deployment accuracy of the starshade Inner Disk Subsystem (IDS).

I.B. Objective and Approach

Milestone 7C of the S5 activity reads:[4]

> Inner Disk Subsystem with optical shield assembly that includes *deployment critical features* demonstrates repeatable deployment accuracy *consistent with* a total pre-launch petal position accuracy within ± 300 µm.

A number of error sources, of which deployment is just one, contribute to this petal position accuracy requirement of ±300 µm. This requirement is sub-allocated to the chief components of the petal position accuracy error (radial bias, radial random, and tangential random), as shown in Table 1. Based on the current best estimates of hardware performance, the components of the petal position accuracy error are further sub-allocated across two activities. The allocation to Milestone 7C (and the related follow-on Milestone 7D) is 30 µm of radial bias, 150 µm of radial random, and 120 µm of tangential random petal position accuracy error. The remainder covers the truss bay thermal cycle stability and any dimensional changes due to e.g. material creep from long-term stowage (which is addressed by Milestones 7A and 7B). For Milestone 7C, the petal position accuracy errors are understood to apply at the petal attachment hinges. The accuracy error components are written as 3σ values, and add in quadrature (root-sum-square), since the error distributions are expected to be random and independent.

	RSS total (µm)	**MS 7A, 7B** (µm)	**MS 7C, 7D** (µm)
Radial bias	130	125	35
Radial random	230	175	150
Tangential random	142	75	120
Total	300		

Table 1: Sub-allocation of the petal position accuracy error to its chief components.

Two previous efforts have demonstrated sufficient deployment repeatability, but with lower fidelity perimeter truss prototypes.[8,9] The prototype tested here has higher-fidelity spokes (with e.g. high thermal stability) and includes a co-deployed optical shield. This marks the first time the IDS has been tested with an integrated optical shield. The optical shield is designed to have zero strain when stowed and fully deployed; therefore, it is not expected to significantly affect IDS deployment accuracy.

The verification approach is to measure the deployed perimeter truss shape after multiple deployments in ambient laboratory conditions with gravity compensation fixtures. The controlled deployment is quasi-static, such that air drag is not a factor.

This paper is organized as follows. Section II describes the starshade flight designs at a high-level. Section III describes the test article and how it deviates from the flight design. Section IV describes the test equipment, including metrology and gravity compensation. Section V describes the test procedures. Section VI presents the test results and data analysis. Section VII discusses the results and Section VIII presents conclusions.

II. Starshade Design

The S5 Technology Development Plan[4] uses the Starshade Rendezvous Mission (SRM) concept as a baseline design. As shown in Figure 1, the SRM design is 26 m in diameter, with 24 8 m-long petals, and

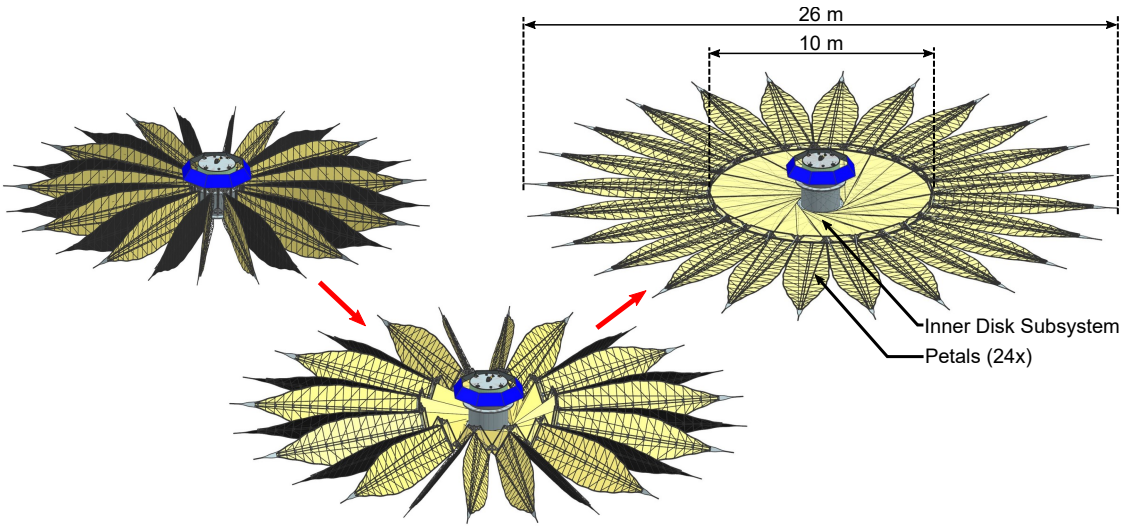

Figure 1: The Starshade Rendezvous Mission (SRM) design. The sequence of images shows the second stage of starshade deployment: IDS unfolding. The petals are fully unfurled before this stage begins.

a 10 m-diameter inner disk.[10] The SRM concept is to launch a starshade in the late 2020s to rendezvous with the WFIRST space telescope at the Sun-Earth L2 point. The starshade for the Habitable Exoplanet Observatory (HabEx) concept[11] uses the same architecture as the SRM starshade, but is double in size – 52 m in diameter with 24 16 m-long petals and a 20 m-diameter IDS. The work presented here is full-scale for the SRM concept, and half-scale for the HabEx starshade.

The mechanical architecture of the "wrapped" starshade design has been described before;[8,9,12] here it will be summarized in brief. The starshade consists of a number of petals attached to the Inner Disk Subsystem (IDS). The IDS stows to a barrel-like shape around which the petals are wrapped. Deployment consists of two steps: first, the petals unfurl, and second, the IDS unfolds. During the first step of petal unfurling, the IDS remains latched in position and does not actuate. During the second step of IDS unfolding (as shown in Figure 1), the petals are fully deployed and have structural stiffness independent of the IDS. The petals and the IDS are exercised in sequence with a clean interface between them, and thus these two deployment steps can be studied independently.

As shown in Figure 2, the hub sits at the center of the IDS. To the hub are attached a number of spokes that connect the hub to the perimeter truss, which is on the outer circumference of the IDS. When fully deployed, the perimeter truss pulls the spokes into tension; the perimeter truss and the hub then go into compression. As such, the deployed IDS is a stiff preloaded structure, very much like a bicycle wheel. The final component of the IDS is a multilayer optical shield (OS) that rests below all the spokes. The OS makes the IDS opaque and is connected to both the hub and the perimeter truss.

The perimeter truss stows in a circular Z-fold, going from a ring-like form when deployed to a barrel-like shape when stowed. The OS folds in an origami wrapping pattern around the hub, occupying the space between the central cylinder of the hub and the perimeter truss when stowed. For unfolding, a motor on the perimeter truss drives deployment; the optical shield and the spokes are passively deployed as the perimeter truss pulls them out.

III. IDS Test Article

Figure 2 shows an as-designed overview of the IDS testbed, which consists of the IDS test article, metrology hardware, and gravity compensation devices. This section describes the IDS prototype that was designed and constructed for this effort. The following section discusses the metrology hardware and gravity compensation methods. The components of the IDS were realized at different levels of fidelity relative to flight-like hardware: a medium-fidelity perimeter truss, medium-fidelity spokes, and a low-fidelity optical shield. In this testbed, the IDS was oriented telescope-side down.

This apparatus was housed in an Earth-gravity engineering lab environment at a Tendeg facility in

Louisville, Colorado. Testing was conducted in air at approximately 24 °C. The air temperature and relative humidity were monitored but not finely controlled.

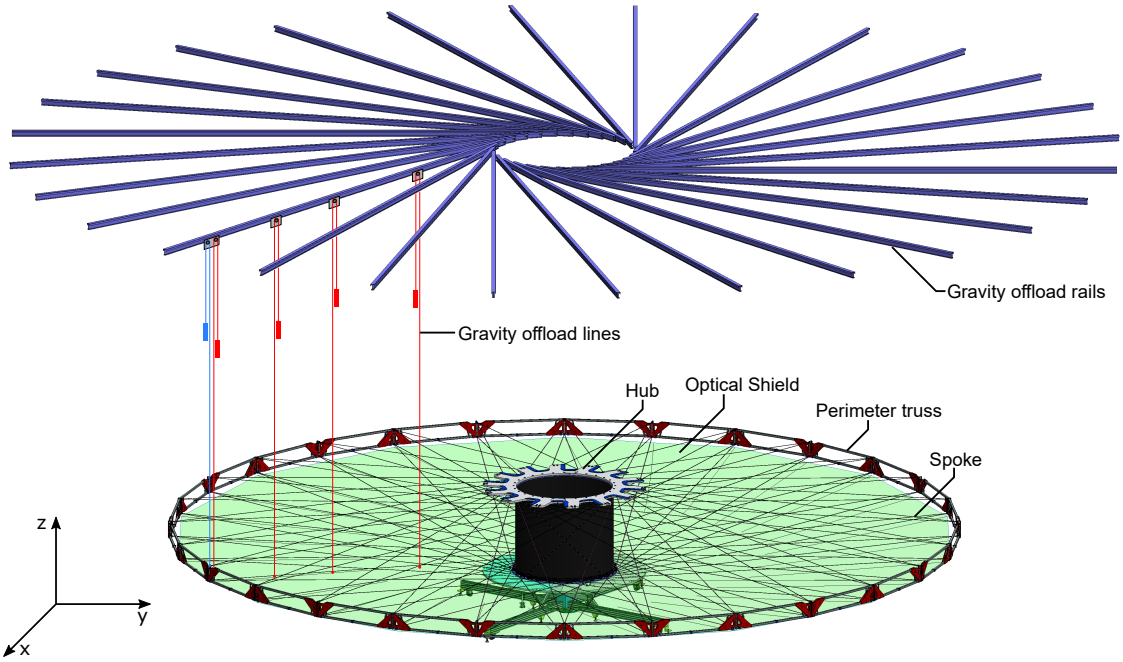

Figure 2: Overview of the IDS testbed. The OS, in green, is transparent for the sake of clarity. Only one set of gravity offload lines are shown, again, for clarity. In reality, each of the 28 gravity offload rails supports four offload lines. The IDS prototype is oriented with the telescope side facing down. The z-axis of the coordinate system is aligned with gravity.

Table 2 compares the key geometrical parameters of the IDS prototype and the SRM IDS. The goal of this experiment was to demonstrate deployment accuracy at full-scale.

Parameter	**IDS prototype**	**SRM IDS**
Deployed IDS diameter	10.6 m	9.8 m
Stowed IDS diameter	2.3 m	2.3 m
Stowed IDS height	1.2 m	1.4 m
Central cylinder diameter	1.3 m	1.6 m
Number of petals	28	24

Table 2: Geometrical parameters of the IDS prototype compared to the SRM design.

One of the key differences between the IDS prototype and the SRM IDS is the number of petals. The SRM design has 24 petals, but the IDS prototype has a perimeter truss designed for 28 petals. This is because the IDS prototype utilizes a 28-sided perimeter truss that was designed and constructed prior to the establishment of the baseline SRM design. To minimize cost and to expedite schedule, this existing perimeter truss was modified and used for this experiment. It is expected that the results from the IDS prototype are applicable to the SRM design. On a local level (i.e. at every unit cell of the rotationally periodic structure), the IDS prototype and the SRM IDS are similar; at a global level, the deployment accuracy of the IDS is not expected to vary between 24 and 28 petals.

Figure 3 shows photographs of the IDS prototype. The following subsections detail the design and construction of the individual components of the IDS prototype: the perimeter truss, the spokes, the hub, and the optical shield.

III.A. Perimeter Truss

The perimeter truss is a stiff structure that reacts the tensile preload of the spokes in the deployed configuration. It provides attachment interfaces for each of the 28 petals. Deployed, it is 10.6 m in diameter. The

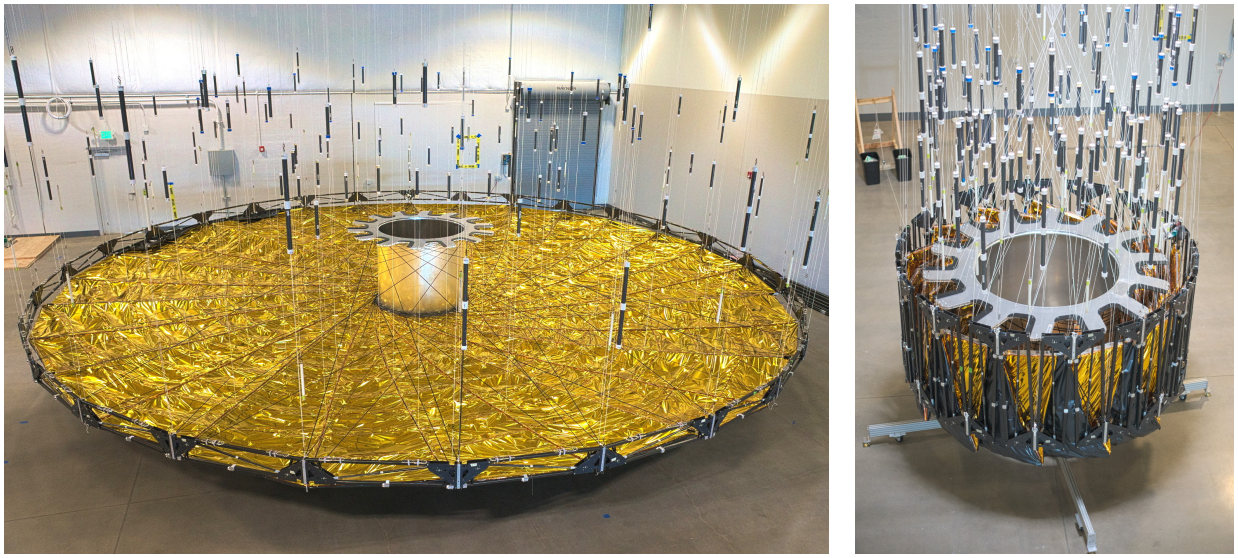

(a) Deployed (b) Stowed

Figure 3: The IDS prototype, deployed and stowed. Deployed, the IDS is 10.6 m in diameter. Stowed, it is 2.3 m in diameter. The two images are not at the same scale. A number of gravity offload counterweights are visible in both images.

starshade perimeter truss draws heritage from the successful Astromesh antenna reflectors.[13]

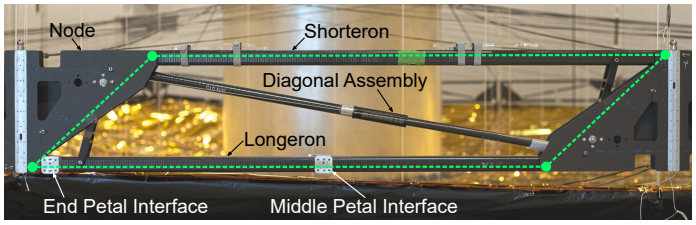

Figure 4: A single perimeter truss bay, showing key components of the four-bar linkage mechanism that actuates each bay. The four-bar linkage is highlighted in green.

The perimeter truss is rotationally symmetric, consisting of 28 bays. Each bay is a four-bar linkage – four rigid members arranged in a planar parallelogram, linked to each other through revolute joints. (A revolute joint is a single-degree-of-freedom joint that allows for free rotation about a fixed axis, e.g. a scissor joint.) Figure 4 shows a single truss bay, with the four-bar linkage highlighted in green. By exercising the shear mechanism of each of the 28 four-bar linkages, the perimeter truss can transition from its deployed ring-like geometry to a stowed barrel-like form, as shown in Figure 5. The longeron and the shorteron[a] are two of the bars of this linkage. They are connected to a node – a stiff triangular structure – at either end through revolute joints. The sides of the nodes form the other two bars of the four-bar linkage.

Along a diagonal of each bay is a pair of telescoping tubes. As this diagonal shortens during deployment, the inner tube slides into the outer tube. Pawls and ratchets on these tubes prevent a bay from being driven backwards. A single braided steel drive cable is strung across all bays; at each bay, it is aligned with the diagonal assembly. Both ends of this cable terminate at a spooler, which uses a motor to drive a capstan that reels in the cable, thus actuating the deployment of the truss. This spooler is housed in a node called the drive node. A flight perimeter truss may include two such drive nodes, located 180° apart, for redundancy and for a more symmetric deployment.

The nodes provide a number of functions: they contain pulleys to route the drive cable, they provide interfaces to the spokes (at each node 4 spokes are attached, 2 near the top of the node, and 2 near the

[a]The term "longeron" is commonly used in structural engineering for a load-bearing member in a framework. The term "shorteron" is specific to this starshade design: a shorteron is similar to a longeron, except shorter; hence "shorteron".

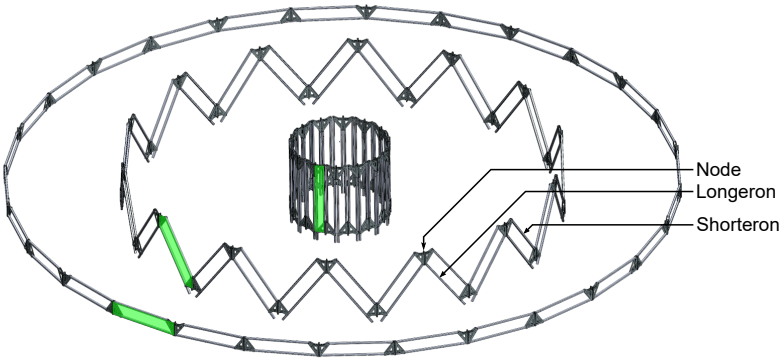

Figure 5: Folding and deployment kinematics of the perimeter truss. A single bay is highlighted in green. Note that the diagonal assemblies are omitted in this figure.

bottom), and the nodes also contain synchronization gears that mechanically link adjacent bays. These gears ensure that the actuation of one bay causes adjacent bays to also actuate, thus synchronizing all bays during deployment. The synchronization gears disengage in the final roughly 10% of deployment. This is because the drive mechanism is sized to drive bays to full deployment in sequence, as opposed to driving bays to full deployment synchronously.

The petal interfaces are bonded to the longerons. In flight, each longeron would have three petal interfaces bonded to it, one in the middle, two at the ends. It was necessary to remove one of the end petal interfaces from each longeron during the process of modifying the truss. (As mentioned previously, a pre-existing perimeter truss was utilized for this experiment; it was modified by constructing new, wider nodes in order to increase the deployed diameter and the stowed diameter to more closely match the SRM geometry.) As such, in this experiment, each longeron has two petal interfaces: one in the middle, one at the end, as shown in Figure 4.

In flight, hinges at the base of a petal would be attached to the three petal interfaces in a quasi-kinematic fashion. For the present experiment, precision parts that stood in for the petal hinges were used instead. These petal hinge stand-ins were shimmed, as the flight petals would be, and their locations were measured after each deployment using metrology targets affixed to them.

In this testbed, the longerons and shorterons were off-the-shelf square-cross-section tubes made from carbon-fiber reinforced plastic (CFRP) material (HR40 fibers with epoxy resin). Petal interfaces were bonded to the longerons in a precision jig, ensuring uniformity of petal interface placement over the truss.

The nodes were assembled from off-the-shelf CFRP plates (HR40 fibers with epoxy resin) and a central aluminum I-beam. The nodes were bonded together using room-temperature-cure epoxy. A precision jig was also used during this bonding process, ensuring a dimensionally uniform population of nodes.

The total perimeter truss mass was 55 kg.

The perimeter truss was built and assembled by Tendeg, LLC in Louisville, Colorado using parts from a pre-existing perimeter truss built at JPL.

III.B. Spokes

The spokes are pulled into tension when deployed and provide a uniform tension field within the IDS to hold the deployed perimeter truss. Ensuring uniform spoke tension, uniform spoke length under the nominal preload, and uniform spoke stiffness is important for deployment accuracy. This testbed has 4 spokes attached to every perimeter truss node, for a total of 112 spokes. The nominal spoke preload in the deployed state is 71 N (16 lbf). Figure 6 shows the lacing pattern used for this testbed.

The 5.2 m-long spokes are comprised of a unidirectional CFRP tape 6.35 mm wide and about 0.10 mm thick. The carbon fibers in this tape are arranged along the length of the spoke. The CFRP material is IM7 carbon fiber in a PEKK (polyether ketone ketone) matrix. At either end of each spoke, two metal end-tabs are bonded using PEI (polyetherimide) resin to the CFRP tape, one on either surface of the tape. These metal end-tabs provide interfaces to the structural hub on one end and to the perimeter truss on the other end of the spoke. On each end, a reamed hole through the two metal end-tabs provides a means of attaching the spoke to a pin or a shoulder bolt. Figure 7 shows two spokes attached to a truss node.

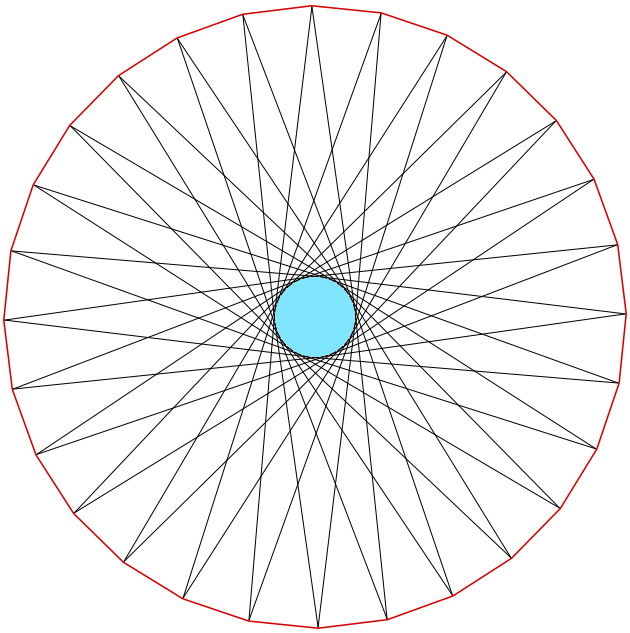

(a) Top view

(b) Side view

Figure 6: Spoke lacing pattern. Four spokes are attached to each perimeter truss node, two at the top, two at the bottom. The spokes are attached to the hub such that the tensioned spoke is tangential to the hub cylinder. At each node, the two top spokes are routed to the top of the hub, and the two bottom spokes are routed to the bottom of the hub.

The spoke CFRP tape is protected by a flexible braided PEEK (polyether ether ketone) sheath. This sheath was designed to not share any of the pre-tension in the spoke; such load-sharing would induce a variation in spoke stiffness throughout the spoke population. To prevent this load-sharing, the spoke sheath was bonded to the end-tabs at either end of the spoke using compliant adhesive-lined shrink tubing.

The spokes were manufactured using a custom-built jig. This jig holds the CFRP tape in a horizontal orientation at the nominal tension of 71 N while the metal end-tabs are bonded to the CFRP tape. A precision Invar bar 5.2 m in length was used to provide precise separation between the ends of the spoke, thus producing a population of 120 spokes with a very low variation in length. (Note that while 120 spokes were manufactured, only 112 are needed for the testbed; the remaining 8 were spares.)

As manufactured, the average spoke length at the nominal tension was 5209.616 mm with a standard deviation of 0.054 mm. The average spoke stiffness EA at the nominal tension was 90.13 kN with a standard deviation of 8.09 kN. This low spread in spoke length and spoke stiffness is beneficial in obtaining an IDS that deploys sufficiently repeatably.

The spokes used for this IDS prototype represent an increase in fidelity over previously tested spokes,[8,9] which were manufactured using braided steel cable. Unlike braided steel spokes, the present spokes have low CTE (measured to be $-0.33 \times 10^{-6}\,^{\circ}\mathrm{C}^{-1}$ at 20 °C) suitable for flight. Additional work is required, however, to decrease the spread in spoke stiffness.

The total spoke mass, including interfaces to the truss, was 2 kg.

The spokes were developed and manufactured by Roccor, LLC in Longmont, Colorado.

III.C. Structural Hub

As shown in Figure 8, the structural hub consists of a central cylinder, two spoke rings, and two truss flanges. Each spoke ring is a precision part to which 56 spoke interfaces are attached. The spoke rings are bonded to the central cylinder, which is a rolled thin-walled aluminum tube. The central cylinder was not held to tight

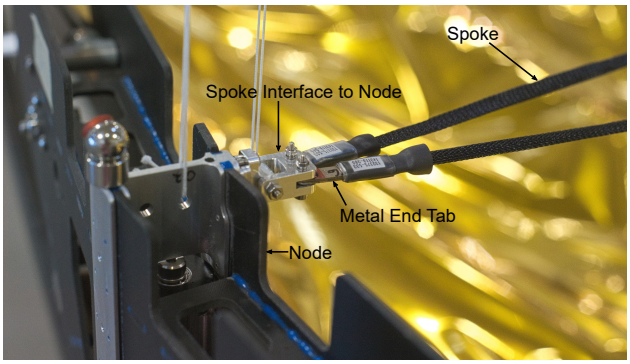

Figure 7: Interface between two spokes and a perimeter truss node.

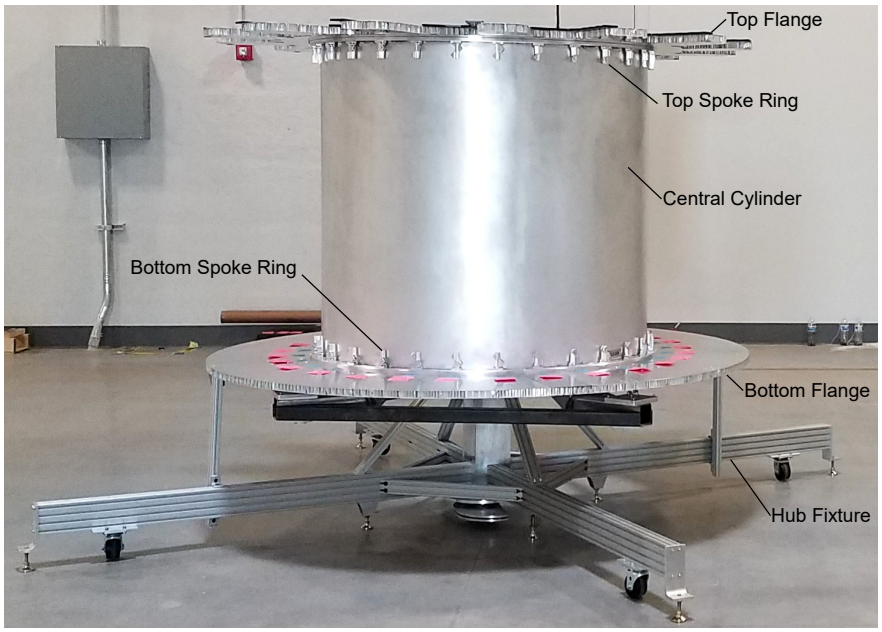

Figure 8: The structural hub and the hub fixture.

tolerances. As such, during the bonding of the spoke rings to the central cylinder, the relative positions of the top and bottom spoke interfaces were measured and the spoke rings were shimmed to ensure alignment between them. The truss flanges are aluminum honeycomb panels that provide a strong and stiff structure to which the stowed perimeter truss can be attached for launch. They do not interface directly with the spokes, and, as such, they were not designed to the tight tolerances associated with the spoke rings.

Once the hub was fully assembled, the location of the 112 spoke interfaces was measured and shimmed to minimize variations in deployed spoke lengths. Assuming a perfect truss, the hub spoke interfaces were shimmed such that the spoke lengths would be within $\pm 200\,\mu m$ of the mean manufactured spoke length.

A more flight-like hub would include launch-restraint latches to hold the truss fixed in its fully stowed position. However, these latches were not included in the present hub, since these are not critical to the deployed shape or deployment accuracy of the IDS.

The hub sits on top of a fixture that restrains all translational degrees of freedom and rotational degrees of freedom about the x- and y- axes, but allows free motion about the z-axis. This fixture is further described in Section IV.A.

The hub and the hub fixture were designed, manufactured, and assembled by Roccor, LLC in Longmont, Colorado.

III.D. Optical Shield

The optical shield (OS) is a multi-layer structure that forms the primary light-blocking element of the IDS. As shown in Figure 9, its global shape is a right circular cone with an opening angle of 169°, with an outer diameter of 10.5 m, and a 1.5 m-diameter inner cutout where the OS interfaces with the central hub. Stowed, it is 2.2 m in diameter.

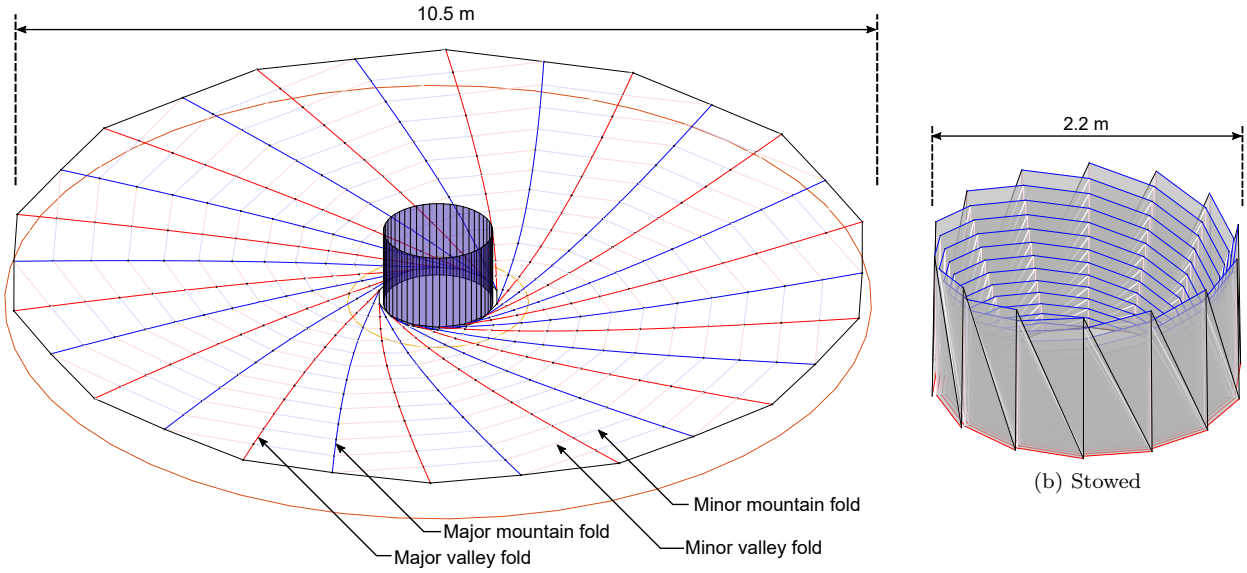

(a) Deployed

(b) Stowed

Figure 9: Isometric views of the OS fold pattern, deployed and stowed. The deployed OS is conical, and the stowed OS consists of spiral wraps that account for the OS panel thickness.

The optical shield consists of a number of planar panels hinged together with revolute joints. The hinges between the panels allow the optical shield to be folded into a compact configuration for launch. The placement of the hinges (i.e. the fold pattern) was designed using a modification of an existing origami-pattern-generation algorithm.[14,15] This modified algorithm generates fold patterns that enable conical surfaces to wrap compactly, while accounting for panel thickness in the folded configuration. This algorithm also guarantees that the fold lengths are the same in the deployed and the stowed configurations, i.e. that the structure is strain-free when deployed and stowed.

Figure 9 shows the OS fold pattern, deployed and stowed. The fold pattern consists of 28 major fold lines: 14 major valley fold lines (dark red in Figure 9a) and 14 major mountain fold lines (dark blue in Figure 9a). The major fold lines fold nearly 180°. There are also a number of minor fold lines (shown as the light lines in Figure 9a) that fold nearly $360°/28 = 12.86°$.

Figure 10 shows the construction of the OS. The panels, which are triangular or quadrilateral in shape, consist of an aluminum frame along the perimeter to which a 16 mm-thick blanket is attached. The aluminum frame for each quadrilateral panel is made of four beams 16 mm tall and 1 mm thick. The blanket consists of two layers of 25 µm-thick Kapton separated by a layer of 16 mm-thick polyurethane foam. The layer of polyurethane foam was lightweighted by cutting out a hexagonal grid of circles from the foam.

As shown in Figure 10, aluminum ribs were placed along all major fold lines. These ribs were constructed from aluminum bars, 1 mm thick and 32 mm tall, hinged together at discrete locations.

The innermost ring of the OS was pinned to the hub. The outermost ring of the OS was attached to the perimeter truss nodes using lengths of cable. These lengths of cable are slack in the deployed configuration; thus, the OS imparts no tension loads to the deployed perimeter truss. The reduction of such loads was a key driver of the OS design; such loads could potentially alter the spoke preload and thus affect the deployed position of the petal interfaces. For ground testing, this requires that the OS weight is sufficiently offloaded, such that no significant loads are transmitted to the perimeter truss. The frames and the ribs – the internal framework of the OS – increase the OS out-of-plane bending stiffness greatly, which aids offloading. Section IV.A describes the gravity compensation systems in detail.

In flight, the interface between the OS and the perimeter truss will include opaque closeouts. Four of

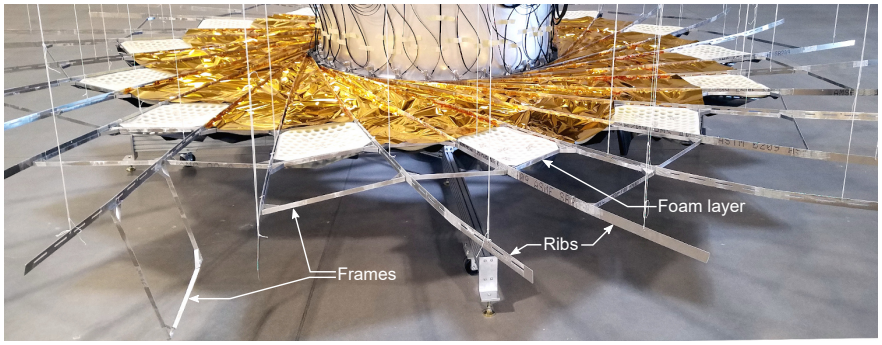

Figure 10: The OS during construction, showing the internal structure. A number of aluminum frames can be seen without integrated blankets. The ribs extend beyond the shown frame network. The construction of the blankets can also be seen.

the truss bays in this prototype had prototypical closeouts between the OS and the perimeter truss. These closeouts were constructed from swaths of Kapton attached to both the perimeter truss and the outermost panels of the OS. These swaths were designed to be slack in the deployed configuration. The higher-fidelity OS that will be constructed to meet the follow-in Milestone 7D will include similar closeouts at every bay.

The total OS mass was 65 kg.

The optical shield was manufactured by Tendeg, LLC in Louisville, Colorado based on designs from JPL.

IV. Test Apparatus

This section describes the gravity compensation methods used to support the IDS prototype and the metrology tools used to measure its deployed shape.

IV.A. Gravity Compensation

To simulate the deployment of the IDS prototype in zero gravity and to ensure that the deployed shape is comparable to the in-space deployed shape, gravity offloading was used to reduce the effects of Earth gravity. The structure was gravity offloaded at 140 discrete locations: lines were attached to the structure at these points, routed over low-friction pulleys, and attached to counterweights. These low-friction pulleys were affixed to wheeled carts that were free to move along 28 overhead rails, as shown in Figure 2. Gravity offload was present throughout the deployment process.

The rail-and-cart system was placed approximately 5 m above the perimeter truss. This height reduces the magnitude of side loads on the structure due off-vertical offload lines.

As shown in Figure 2, four offload points were used for each OS major fold line. The locations of these points along the fold line were chosen to minimize the out-of-plane deflections of the OS in the deployed state; the sum of the OS counterweights amounted to the total OS weight. One offload point was used for each truss node. The counterweight at each node was $1/28^{\text{th}}$ the weight of the entire truss, except for the drive node, which had additional counterweight to account for the spooler hardware.

The structural hub was held by a fixture that restrained, relative to the ground, all translational degrees of freedom and the rotational degrees of freedom about the x- and y- axes. The rotational degree of freedom about the z-axis was left free; the hub needs to rotate relative to the perimeter truss during deployment as the OS is unwrapped. The hub fixture is shown in Figure 8.

As can be seen in Figure 3b, the top flange of the hub had cutouts to allow, in the stowed configuration, three of the four OS offload lines to pass through. When stowed, the OS offload lines are vertical immediately above the OS (and thus impart no side loads onto the stowed OS), but are deflected in an off-vertical direction by the hub top flange, as they go to their respective offload carts. This imparts a deployment-aiding torque on the hub about the z-axis. Therefore, a counter-torque mechanism was implemented to impart an opposing torque such that the net external torque on the hub was zero. The counter-torque mechanism consists of a cam, attached to the rotating portion of the hub fixture, to which a force is applied by means of a constant-force spring and a hanging weight. The profile of the cam was designed to match the varying torque generated by the OS offload lines on the rotating hub.

IV.B. Metrology

A Leica AT402 laser tracker[16,17] was used to measure the 3D location of the centers of spherically mounted retroreflectors (SMRs) affixed to the IDS prototype. The AT402 laser tracker comprises an absolute distance meter (ADM) mounted on an azimuth/elevation rotary stage. The ADM measures the range to the SMR, and two angular encoders on the rotary stage measure azimuth and elevation. Thus, the laser tracker can measure the 3D location of the center of an SMR. An SMR consists of a hollow corner-cube retroflector mounted in a 12.7 mm-diameter steel sphere, such that the apex of the corner cube is coincident with the center of the sphere. The laser tracker also has an integrated weather station that records air temperature and relative humidity at the time of each measurement.

Laser trackers have sufficiently small measurement uncertainties for this experiment. The stated maximum permissible error of the AT402 laser tracker is $\pm\,(15\,\mu\text{m} + 6\,\mu\text{m/m}$ of measurement range).[16] In practice, however, the laser tracker reports an uncertainty for each measurement, and the 3σ uncertainty was approximately half the maximum permissible error for the same range. For each measurement, the laser tracker takes 1000 samples over approximately 2 seconds; the reported uncertainty is calculated based on the spread of these samples.

The laser tracker was placed approximately 1.5 m away from the edge of the deployed perimeter truss, and elevated approximately 3.2 m above the ground using an aluminum tripod affixed atop a wood platform. The elevation allowed for a clear view of the SMRs on the far side of the truss, unobscured by the hub.

A number of SMRs were affixed to the test hardware. Of these, the laser tracker could reliably see a total of 67 SMRs:

- 22 SMRs attached to the middle petal interfaces on the truss longerons,
- 12 SMRs attached to the end petal interfaces on the longerons,
- 26 SMRs on the tops of the node,
- 3 SMRs on the hub, and
- 4 SMRs fixed to the floors and the walls of the room as reference markers.

A number of other SMRs were obscured by test hardware – offload lines, offload weights, spokes, or the perimeter truss itself. Despite this, there were no large gaps between measured locations on the perimeter truss: 25 of the 28 longerons had at least one of their petal interface locations measured, and 10 of the 28 longerons had *both* petal interface locations measured. Figure 11 shows the locations of the measured SMRs.

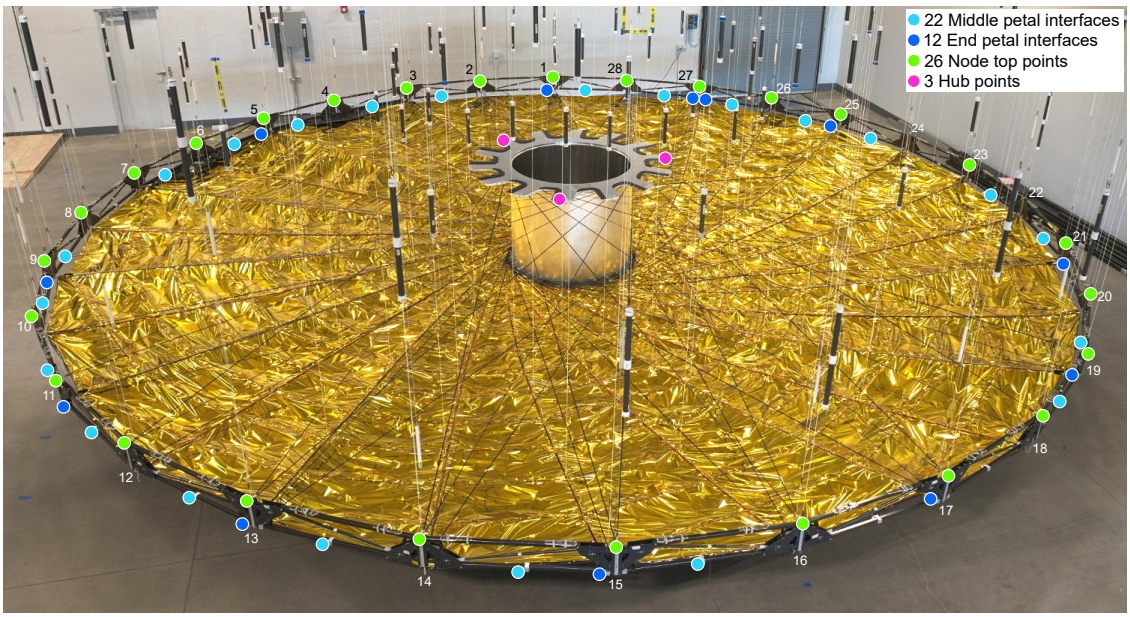

Figure 11: Measured SMRs on the IDS prototype. The numbering of the nodes and the adjacent longerons is indicated; node 1 is the drive node.

V. Test Procedures

A total of 58 deployments of the IDS prototype were conducted between 13 June 2019 and 21 August 2019. About 10 of these were for initial verification of functionality, and 26 of these were to conduct shimming of the petal interfaces. The remaining 22 deployments were performed in the final shim state. The following subsections describe the procedures used for shimming the location of the petal interfaces, and for stowing and deploying the IDS.

V.A. Shimming

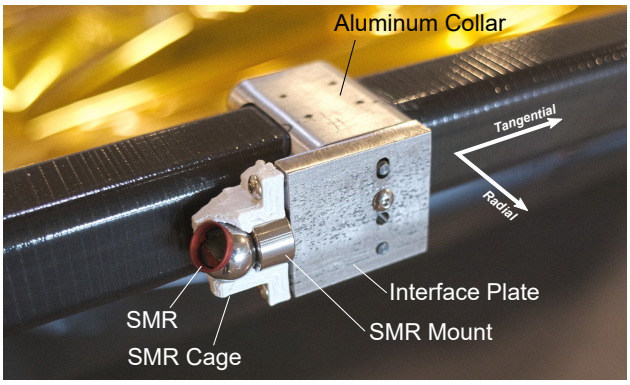

Figure 12: SMR attachment to the petal interface on the longeron. The SMR location could be shimmed in the radial and tangential directions by adjusting two independent shim stacks.

Figure 12 shows a middle petal interface with an SMR and the components necessary to shim its in-plane location. Identical components were attached to all 56 petal interfaces on the perimeter truss. The aluminum collar is bonded to the longeron; in flight, a petal hinge would be attached to this collar. In this experiment, an interface plate was affixed to the aluminum collar. The SMR locations were shimmed as the petal hinges would be for flight. Metal shims were inserted between the interface plate and the aluminum collar to adjust the radial position of the SMR. To the interface plate is attached an SMR mount; a shaft on the SMR mount inserts into a corresponding hole in the interface plate. Metal shims between SMR mount and the interface plate were used to adjust the tangential position of the SMR. The SMR is magnetically affixed to the SMR mount, and the SMR cage preloads the SMR mount against the interface plate and protects the SMR from being accidentally bumped. The SMR cage contacts only the SMR mount, and not the SMR itself.

Eight rounds of measurement and shim adjustment were performed. For each round of measurement, at least 3 deployments were conducted, establishing a mean deployed position for each SMR. Based on these measured deployed locations, shim corrections were computed and implemented. The decision to stop after eight rounds of shimming was partially based on schedule; additional shimming rounds could have been performed to reduce shape errors. The minimum shim thickness used was 25.4 µm; this set the resolution of the shim corrections.

V.B. Stowage and Deployment

The IDS prototype was stowed manually. Ratcheting mechanisms based on vernier scales were attached to the perimeter truss bays and were used to synchronize the truss bays to each other during the first few percent of stowage. These mechanisms were removed after the synchronization gears built into the nodes engaged with each other, at roughly 10% of the way through stowage.

A torque was applied to the hub to cause the OS to wrap around the hub as the truss diameter was decreased. This torque was reacted by tension in the perimeter truss drive cable – the torque acted to stow the IDS and the drive cable acted to unstow it. As the drive cable was slowly slackened, the torque caused the hub to rotate and the IDS to stow. This method allowed for a slow and controlled stow process.

Half of the 112 spokes, the ones that roughly follow the major fold lines of the OS, were wrapped with the OS. These spokes are on left side of each node, looking inwards to the hub. The other half of the spokes, on the right side of the nodes, developed slack during stowage. This slack was managed by counter-wrapping the spokes in a "spoke bag", as shown in Figure 13. These bags were constructed from plastic sheets bonded

together, with two openings at either end through which the spoke was passed. By counter-wrapping the spoke within this bag, slack could be effectively managed without exceeding the minimum bend radius of the spokes. During deployment, these spokes slowly unwrapped.

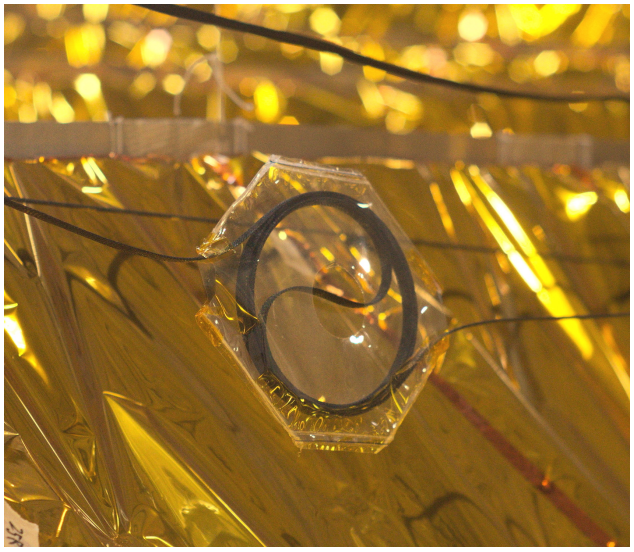

Figure 13: A spoke partially wrapped in a spoke bag during deployment. Tension on either of the two segments of the spoke exiting the bag causes the spoke to unwrap.

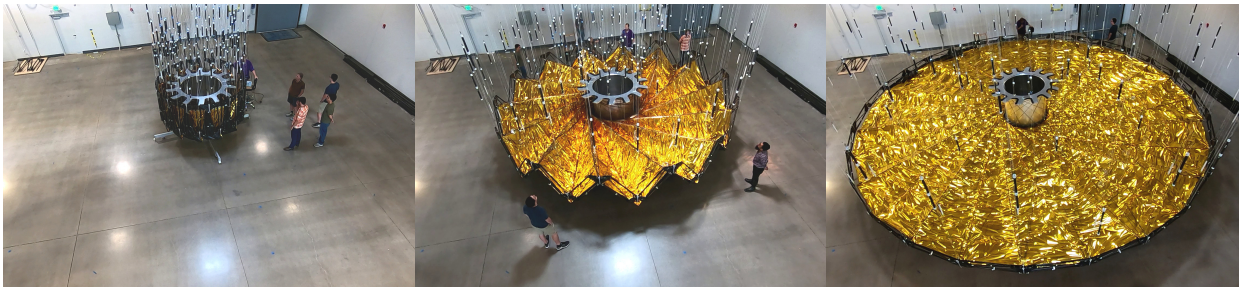

(a) 96% stowed (b) Mid deploy (c) Fully deployed

Figure 14: Deployment from a 96% stowed state. The images are at the same scale.

22 deployments (see Table 3) were performed with the final shim state. A number of these deployments started from a partially stowed state. This was to save time: a full stow of the IDS prototype takes about 5 hours, whereas a 8% partial stow takes only a half an hour. Also, it was expected that partial deployments would be representative of full deployments in terms of deployment repeatability, since the final deployed position of the IDS is set only in final few percent of deployment. This expectation was confirmed by the measured data, as discussed in Section VII.A.

The degree of stowage is quantified as a stow percent s, which is defined as the angle between the longerons when stowed, divided by 180°, which is the angle between the longerons when fully stowed:

$$s = \frac{\theta_{longerons}}{180^\circ} \times 100\% \tag{1}$$

Thus $s = 0\%$ is fully deployed and $s = 100\%$ is fully stowed. Of the 22 deployments listed in Table 3, 11 were from 8% stowed, 3 from 49% stowed, 3 from 82% stowed, and 5 from 96% stowed.

The IDS was not stowed to 100% since the hub did not have the requisite launch-restraint latches to capture the fully stowed truss. However, as shown in Section VII.A, the deployment accuracy of the IDS does not change with the degree of stowage. Additionally, unlike the Astromesh reflector, the starshade IDS has no strain energy when fully stowed and, as such, it does not exhibit a dynamic first motion.

	Timestamp	Stow %
1	2019.07.17 14:38	8
2	2019.07.17 17:05	8
3	2019.07.17 18:21	8
4	2019.07.17 19:37	8
5	2019.07.18 09:05	8
6	2019.07.18 17:24	82
7	2019.07.22 10:36	8
8	2019.07.22 12:13	8
9	2019.07.22 13:40	8
10	2019.07.22 15:14	8
11	2019.07.23 10:00	8
12	2019.07.24 13:56	82
13	2019.07.25 12:56	82
14	2019.07.25 16:25	49
15	2019.07.26 14:07	49
16	2019.07.29 13:22	49
17	2019.08.08 11:47	8
18	2019.08.12 17:12	96
19	2019.08.15 13:47	96
20	2019.08.16 14:16	96
21	2019.08.20 13:04	96
22	2019.08.21 11:46	96

Table 3: List of deployments in the final shim state.

During deployments, the IDS prototype was not touched. Occasionally, the offload counterweights would tangle with each other, or be wrapped around their offload lines. These tangles were undone using a long pole; the deployment was paused while these counterweights were untangled.

Deployments from the 96% stow state took about 25 minutes. This slow, quasi-static deployment rate was chosen to reduce the effects of air drag and to simplify future efforts to numerically model the IDS deployment. Figure 14 shows three stills from a video of a deployment from a 96% stow state.

VI. Test Results and Data Analysis

VI.A. Data Processing

At the end of each deployment, the location of the SMRs was measured, in sequence, by an automated program. This automated program was run 3 times at the end of each deployment, thus taking 3 independent passes. The canonical deployed location of each SMR was taken to be the mean of the measurements from the 3 passes. This reduces random transient sources of error (e.g. temporary obscuration of the laser tracker aperture, air turbulence, building vibrations).

All measured SMR locations after a deployment were translated and rotated as a rigid body to best fit (in a least squares sense) the measured petal interface locations to the nominal petal interface locations. It is required that the petals be placed at the nominal location in *some* coordinate frame, not necessarily one tethered to the hub or the spacecraft bus. This rigid-body transformation preserves petal interface locations relative to each other.

VI.B. Definitions of Shape Error

The measured location of the SMR at the i^{th} petal interface at the j^{th} deployment is denoted by $\boldsymbol{p}_{ij}$, which is a three-dimensional vector. i is an integer between 1 and 34, the total number of measured petal interfaces; and j is an integer between 1 and 22, the total number of deployments. $\overline{\boldsymbol{p}}_i$ is the mean deployed location (taken over the 22 deployments) of the i^{th} petal interface. The nominal petal interface positions are denoted

by $\boldsymbol{p}_i^*$. These nominal petal interface positions are defined based on a perfect 28-sided polygon centered at the origin, and lie in the x, y plane.

There are two measures of shape error that are of interest: accuracy, which is the deviation between the measured locations $\boldsymbol{p}_{ij}$ and the nominal location $\boldsymbol{p}_i^*$; and repeatability, which is the deviation between the measured locations $\boldsymbol{p}_{ij}$ and the mean deployed location $\overline{\boldsymbol{p}}_i$. Figure 15 illustrates the relation between these values. Both accuracy and repeatability are measures of variation in shape from deployment to deployment; however, accuracy includes a contribution from shimming errors which are secular biases that do not vary between deployments, whereas repeatability is insensitive to these shimming errors. To meet Milestone 7C, three components of the shape accuracy error – radial bias, radial random, and tangential random – must fall within the allocated bounds in Table 1.

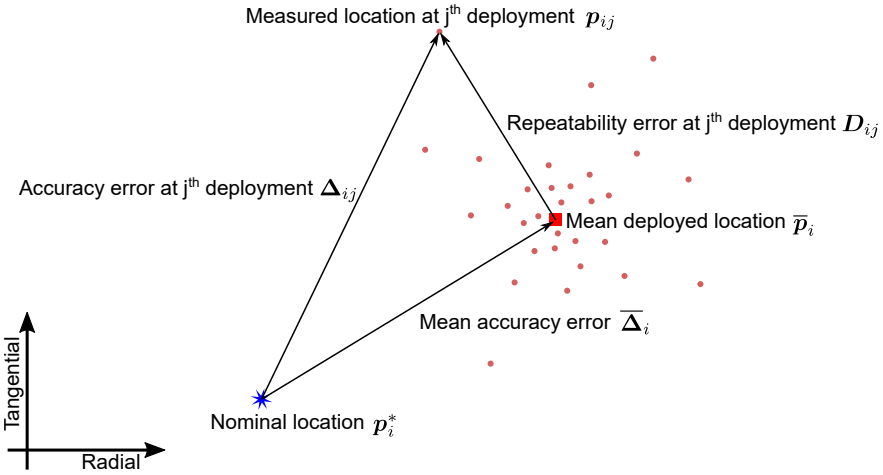

Figure 15: Definitions of the two measures of error: accuracy and repeatability.

VI.C. Radial and Tangential Accuracy

As shown in Figure 15, the accuracy error $\boldsymbol{\Delta}_{ij}$ is defined as the difference between the measured location $\boldsymbol{p}_{ij}$ and the nominal location of the i^{th} petal interface $\boldsymbol{p}_i^*$:

$$\boldsymbol{\Delta}_{ij} = \boldsymbol{p}_{ij} - \boldsymbol{p}_i^* \tag{2}$$

Of interest are the radial and tangential components of the accuracy error $\boldsymbol{\Delta}_{ij}$; the distribution of these is compared against the radial random and tangential random allocations in Table 1. The local radial and tangential basis vectors $\hat{\boldsymbol{r}}_i$ and $\hat{\boldsymbol{t}}_i$ for the i^{th} petal interface are defined using the nominal location of the petal interface $\boldsymbol{p}_i^*$:

$$\hat{\boldsymbol{r}}_i = \frac{\boldsymbol{p}_i^*}{\|\boldsymbol{p}_i^*\|} \qquad\qquad \hat{\boldsymbol{t}}_i = \hat{\boldsymbol{z}} \times \hat{\boldsymbol{r}}_i \tag{3}$$

where $\hat{\boldsymbol{z}}$ is the unit vector along the z-axis, which is perpendicular to the plane that contains the nominal petal interface locations. Using these local basis vectors, the accuracy error $\boldsymbol{\Delta}_{ij}$ can be decomposed into radial and tangential components ΔR_{ij} and ΔT_{ij}:

$$\Delta R_{ij} = \boldsymbol{\Delta}_{ij} \cdot \hat{\boldsymbol{r}}_i \qquad\qquad \Delta T_{ij} = \boldsymbol{\Delta}_{ij} \cdot \hat{\boldsymbol{t}}_i \tag{4}$$

The radial and tangential components over the 22 deployments of the i^{th} petal interface are fitted with normal distributions:

$$\Delta R_{ij} \sim \mathcal{N}\left(\overline{\Delta R}_i, \sigma_{Ri}^2\right) \qquad\qquad \Delta T_{ij} \sim \mathcal{N}\left(\overline{\Delta T}_i, \sigma_{Ti}^2\right) \tag{5}$$

where $\overline{\Delta R}_i$ and $\overline{\Delta T}_i$ are the mean radial and tangential components of the accuracy error of the i^{th} petal interface and σ_{Ri} and σ_{Ti} are the standard deviations. $\overline{\Delta R}_i$ and $\overline{\Delta T}_i$ are the in-plane components of the mean accuracy error $\overline{\boldsymbol{\Delta}}_i$ defined in Figure 15, which is indicative of shimming errors.

The standard deviations σ_{Ri} and σ_{Ti} must be increased to account for the uncertainties in the measured locations. The laser tracker outputs an uncertainty for each individual measurement. Based on these values, a 1σ uncertainty u_i can be computed for each measurement $\boldsymbol{p}_{ij}$. For the present experiment, the 1σ uncertainty u_i ranges between 1 µm and 10 µm for the petal interfaces. The corrected standard deviations $\hat{\sigma}_{Ri}$ and $\hat{\sigma}_{Ti}$ are obtained by taking a root-sum-square of the measured standard deviations and the measurement uncertainties:

$$\hat{\sigma}_{Ri}^2 = \sigma_{Ri}^2 + u_i^2 \qquad\qquad \hat{\sigma}_{Ti}^2 = \sigma_{Ti}^2 + u_i^2 \tag{6}$$

Given the low sample size – 22 deployments in total – the standard deviations of the sample may differ from the standard deviations of the underlying population. To retire this uncertainty, tolerance intervals are employed, following the process set out by.[8] A tolerance interval is a $\pm k\sigma$ region centered around the mean that will contain a fraction γ of future members of a population with a confidence level defined by $(1-\alpha)$. σ is the sample standard deviation, and k is a factor dependent on the number of deployments n, α, and γ. Computing k exactly is challenging; a conservative estimate for k is used:[8,18]

$$k = \sqrt{\frac{(n-1)\chi_{1,\gamma}(1/n)}{\chi_{n-1,\alpha}}} \tag{7}$$

where $\chi_{1,\gamma}(1/n)$ is a quantile from a non-central chi-square distribution, and $\chi_{n-1,\alpha}$ is a quantile from a standard chi-square distribution. A tolerance interval is used that will contain 99.73% of future members with 90% confidence, i.e. $\gamma = 0.9973$ and $(1-\alpha) = 0.90$. $n = 22$ gives $k = 3.8596$ and a tolerance interval of $\pm 3.8596\sigma$. This is a conservative estimate for the $\pm 3\sigma$ region around the mean for a well-sampled normal distribution, which contains 99.73% of the population.

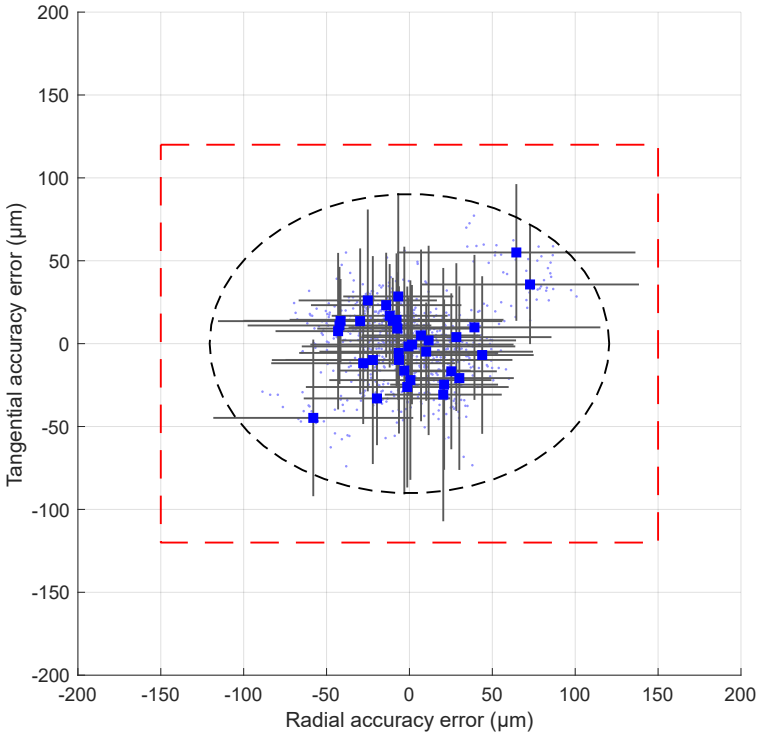

Figure 16: Radial and tangential components of the measured deployment accuracy errors of the petal interfaces. The blue squares represent the mean accuracy errors of the measured petal interfaces, and the bars represent the tolerance intervals around the mean. Accuracy errors of the petal interfaces from individual deployments are shown as light blue dots. The red rectangle represents the radial (150 µm) and tangential (120 µm) accuracy allocations. The major and minor axes of black dashed ellipse represents the 3σ radial and tangential accuracy errors – 121 µm radial and 91 µm tangential – calculated using the Monte Carlo analysis described in Section VI.D.

Figure 16 plots the mean radial and tangential components of the accuracy error $\overline{\Delta R}_i$ and $\overline{\Delta T}_i$, as well as the size of the tolerance intervals around each mean. Figure 17 plots these quantities separately for each of the measured petal interfaces. Additionally, the in-plane components of the accuracy errors $(\Delta R_{ij}, \Delta T_{ij})$ for all i and j are shown in both Figure 16 and Figure 17. A Monte Carlo approach, described in Section VI.D, was used to determine the 3σ levels for the radial and tangential components of the shape accuracy errors across the 34 measured petal interfaces.

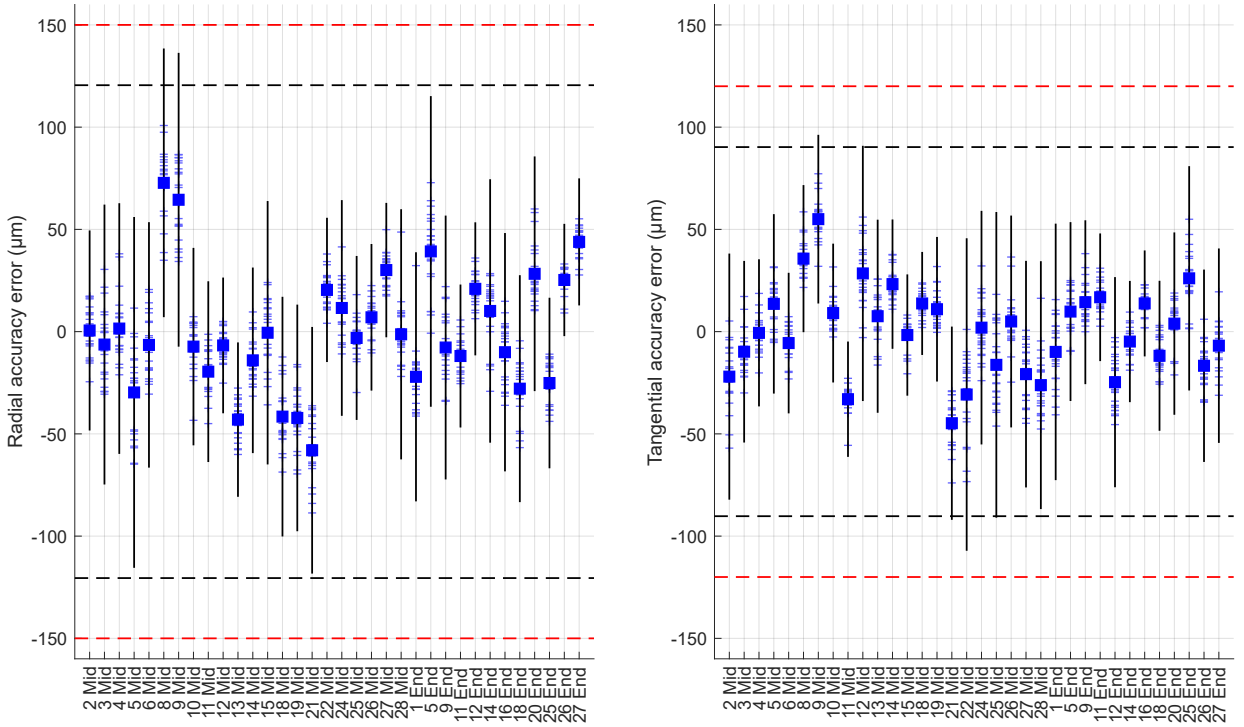

(a) Radial

(b) Tangential

Figure 17: In-plane components of the measured deployment accuracy errors of the petal interfaces, shown separately for each of the 34 measured petal interfaces. The blue squares represent the mean, and the bars represent the tolerance intervals around the mean. Accuracy errors from individual deployments are visible as light blue dashes. The numbering of the petal interfaces is shown in Figure 11. "Mid" represents a middle petal interface on a longeron, and "End" represents an end petal interface. The red dashed lines represent the the radial (150 µm) and tangential (120 µm) accuracy allocations and the black dashed lines represent the 3σ radial and tangential accuracy errors – 121 µm radial and 91 µm tangential – calculated using the Monte Carlo analysis described in Section VI.D.

VI.D. Monte Carlo Calculation of 3σ Accuracy Bounds

A Monte Carlo (MC) analysis was done to estimate the 3σ levels for the radial and tangential components of the accuracy error. As defined in Figure 15 and Equation (16), the experimental accuracy error $\boldsymbol{\Delta}_{ij}$ of the i^{th} petal interface at the j^{th} deployment is the sum of the shimming error i.e. the mean accuracy error $\overline{\boldsymbol{\Delta}}_i$ and the repeatability error $\boldsymbol{D}_{ij}$:

$$\boldsymbol{\Delta}_{ij} = \overline{\boldsymbol{\Delta}}_i + \boldsymbol{D}_{ij} \tag{8}$$

This property was used to generate a population of Monte Carlo accuracy errors. A population of 1000 "shim states" of the IDS was generated; each "shim state" consists of shimming errors $\overline{\boldsymbol{\Delta}}_{MC,ip}$ for each of the 34 measured petal interfaces, $i = 1, 2, ..., 34$ and $p = 1, 2, ..., 1000$. For each "shim state", a population of 1000 deployment repeatability errors $\boldsymbol{D}_{MC,iq}$ was generated for each petal interface, where $i = 1, 2, ..., 34$ and $q = 1, 2, ..., 1000$. This yields a population of 3.4×10^7 Monte Carlo accuracy errors $\boldsymbol{\Delta}_{MC,ipq}$ associated

with the p^{th} "shim state", the q^{th} deployment, and the i^{th} petal interface:

$$\boldsymbol{\Delta}_{MC,ipq} = \overline{\boldsymbol{\Delta}}_{MC,ip} + \boldsymbol{D}_{MC,iq} \tag{9}$$

To generate the 1000 "shim states", the radial and tangential components of the shimming error for each petal interface $\overline{\boldsymbol{\Delta}}_{MC,ip}$ were drawn from zero-mean normal distributions:

$$\overline{\Delta R}_{MC,ip} \sim \mathcal{N}\left(0, \sigma^2_{MC,\overline{\Delta R}}\right) \qquad \overline{\Delta T}_{MC,ip} \sim \mathcal{N}\left(0, \sigma^2_{MC,\overline{\Delta T}}\right) \tag{10}$$

where $\sigma_{MC,\overline{\Delta R}}$ and $\sigma_{MC,\overline{\Delta T}}$ are the estimated standard deviations of the radial and tangential components of the shimming errors. The standard deviations used for the Monte Carlo analysis are larger than the experimentally measured standard deviations, to account for the low sample size ($n = 34$ petal interfaces). The experimentally measured shimming errors are indicated by the blue squares in Figure 16 and Figure 17. Tolerance intervals are used to estimate the Monte Carlo standard deviations. Tolerance intervals with size $\pm k_2\sigma_{exp}$ were calculated that contain that contain 99.73% population with 90% confidence, where σ_{exp} is the experimentally measured standard deviation. Using Equation (7), $k_2 = 3.6358$. These tolerance intervals are comparable to $\pm 3\sigma$ for a well-sampled distribution, since they contain 99.73% of the population. By setting $k_2\sigma_{exp} = 3\sigma_{MC} \Rightarrow \sigma_{MC} = 1.212\sigma_{exp}$, the standard deviations can be estimated for this Monte Carlo analysis. Table 4 lists the experimental and the Monte Carlo standard deviations of the shimming errors.

	σ_{exp} Experimental (µm)	σ_{MC} Monte Carlo (µm)
Radial	29.6	35.9
Tangential	21.3	25.9

Table 4: Shimming error standard deviations

For each Monte Carlo "shim state", 1000 radial and tangential components of the repeatability errors for each petal interface were drawn from zero-mean normal distributions:

$$DR_{MC,iq} \sim \mathcal{N}\left(0, \sigma^2_{MC,DRi}\right) \qquad DT_{MC,iq} \sim \mathcal{N}\left(0, \sigma^2_{MC,DTi}\right) \tag{11}$$

where $\sigma_{MC,DRi}$ and $\sigma_{MC,DTi}$ are the estimated standard deviations of the radial and tangential components of the repeatability errors. These estimated standard deviations are different for each petal interface, and are calculated, as above, using tolerance intervals:

$$3\sigma_{MC,DRi} = k\hat{\sigma}_{Ri} \qquad 3\sigma_{MC,DTi} = k\hat{\sigma}_{Ti} \tag{12}$$

where $\hat{\sigma}_{Ri}$ and $\hat{\sigma}_{Ti}$ are the corrected sample standard deviations and $k = 3.8596$ is the tolerance interval factor; these quantities are defined in Section VI.C. The estimated standard deviations of the repeatability errors used in this Monte Carlo analysis ranged between 9.2 µm and 28.6 µm for the radial component, and between 8.4 µm and 25.5 for the tangential component for the 34 petal interfaces.

This process yields 1000 "shim states" for the 34 petal interfaces; each "shim state" is then "deployed" 1000 times, resulting in a population of 3.4×10^7 radial and tangential components of the accuracy error. The standard deviations of these populations gives the 3σ bounds for the measured accuracy errors: 121 µm for the radial component, and 91 µm for the tangential component. Figure 18 shows the results of this Monte Carlo analysis.

VI.E. Radial Bias

Radial bias is the difference between the deployed radius of the perimeter truss and the nominal radius. The radial bias B_j at the j^{th} deployment can be calculated as the mean of the radial accuracy errors of all the petal interfaces at that deployment:

$$B_j = \frac{1}{34}\sum_{i=1}^{34} \Delta R_{ij} \tag{13}$$

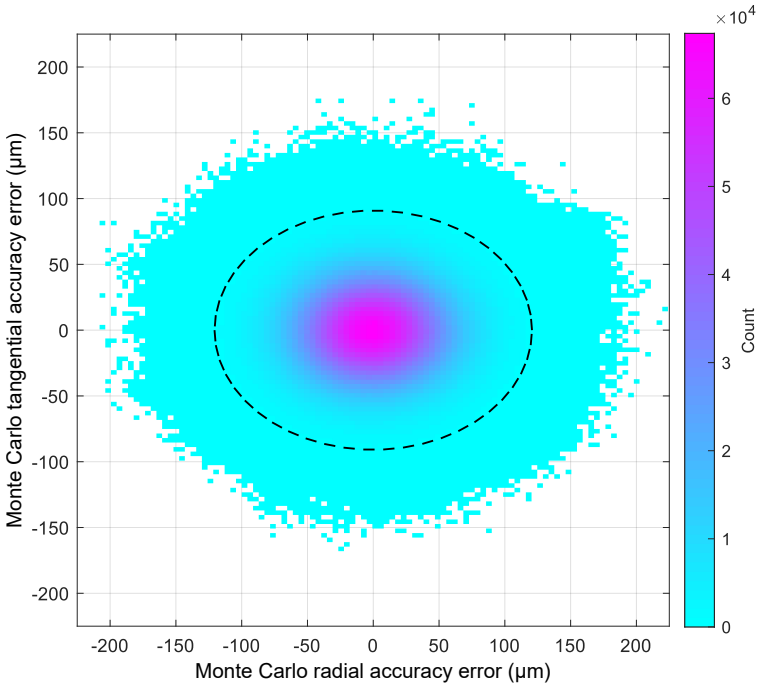

Figure 18: Histogram showing the results of the Monte Carlo analysis. The major and minor axes of black dashed ellipse represents the computed 3σ radial and tangential accuracy errors – 121 µm radial and 91 µm tangential.

The uncertainty in each measurement of the radial bias was calculated to be 1.7 µm at a 3σ level based on the measurement uncertainties u_i of the 34 petal interfaces. Figure 19 plots the radial bias for each of the 22 deployments.

Using the measured data, the radial bias of future deployments can be bounded. The 22 measured radial bias terms are fitted with a normal distribution:

$$B_j \sim \mathcal{N}\left(\overline{B}, \sigma_B^2\right) \tag{14}$$

where $\overline{B}$ is the mean radial bias across the 22 deployments, and σ_B is the standard deviation. The standard deviation σ_B was calculated to be 6.6 µm. This is expanded to account for the measurement uncertainty, resulting in the corrected standard deviation $\hat{\sigma}_B = 6.8$ µm.

As in Section VI.C, to account for the low sample size of 22 deployments, a tolerance interval of size $\pm k\hat{\sigma}_B$ is constructed to place bounds that are equivalent to 3σ levels. $k = 3.8596$ is obtained using the same inputs as Section VI.C ($\gamma = 0.9973$, $n = 22$, $(1-\alpha) = 0.90$). This gives the tolerance interval as ±26 µm.

VI.F. Deployment Repeatability

Based on Figure 15, the repeatability error $\boldsymbol{D}_{ij}$ is defined as the difference between the deployed position after the j^{th} deployment $\boldsymbol{p}_{ij}$ and the mean deployed position over all deployments $\overline{\boldsymbol{p}_i}$:

$$\boldsymbol{D}_{ij} = \boldsymbol{p}_{ij} - \overline{\boldsymbol{p}}_i \tag{15}$$

As defined in Figure 15, the accuracy error $\boldsymbol{\Delta}_{ij}$ is the sum of the repeatability error $\boldsymbol{D}_{ij}$ and the mean accuracy error $\overline{\boldsymbol{\Delta}}_i$:

$$\boldsymbol{\Delta}_{ij} = \boldsymbol{D}_{ij} + \overline{\boldsymbol{\Delta}}_i \tag{16}$$

Thus, the accuracy error $\boldsymbol{\Delta}_{ij}$ arises from deployment repeatability errors $\boldsymbol{D}_{ij}$ that change from deployment to deployment and a mean accuracy error $\overline{\boldsymbol{\Delta}}_i$ that remains constant. The repeatability error $\boldsymbol{D}_{ij}$ therefore is an indication of the deployment accuracy of the structure if the shimming was perfect, i.e. if $\overline{\boldsymbol{\Delta}}_i = 0$.

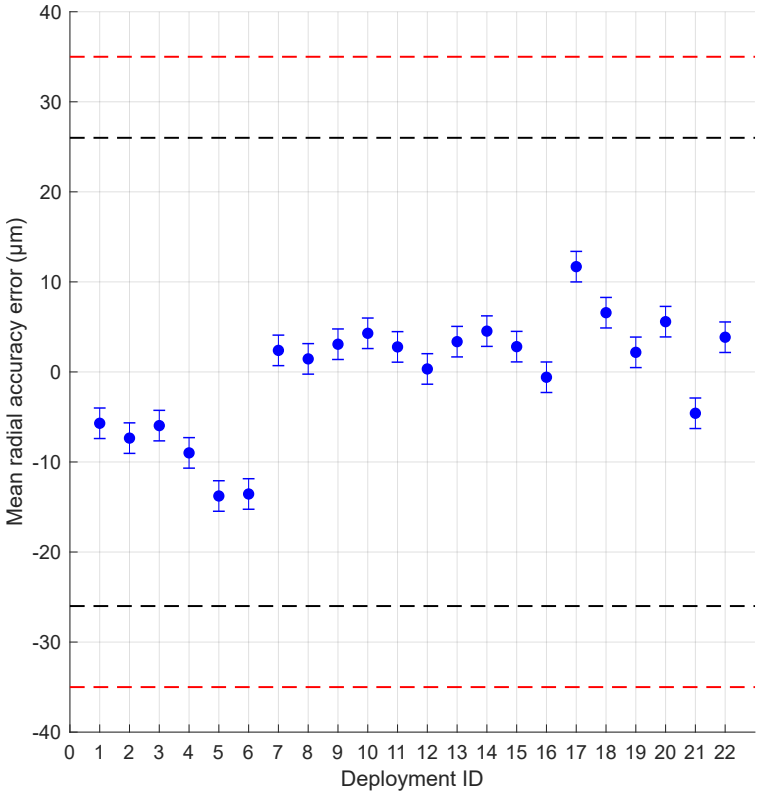

Figure 19: Radial bias errors for each of the 22 deployments. The black dashed lines represent the ±26 µm tolerance interval constructed from the measured data. The red dashed lines represent the ±35 µm allocation.

Now, clearly, perfect shimming is impractical to achieve, but the magnitude of the shimming errors can be reduced.

Taking the standard deviation over all deployments of both sides of Equation (16), it can be seen that $\sigma(\boldsymbol{\Delta}_{ij}) = \sigma(\boldsymbol{D}_{ij})$ since the mean accuracy error $\overline{\boldsymbol{\Delta}}_i$ is constant over all deployments. This means that the size of the tolerance intervals for the repeatability errors $\boldsymbol{D}_{ij}$ is the same as calculated above for the accuracy errors $\boldsymbol{\Delta}_{ij}$.

Figure 20 plots the radial and tangential components of the repeatability error $\boldsymbol{D}_{ij}$. The error bars indicate the maximum radial and tangential tolerance intervals; so 99.73% of the future data is guaranteed to fall within this range with 90% confidence.

VI.G. Out-of-Plane Repeatability

Milestone 7C is understood to apply only to the in-plane components of deployment error. Yet it is useful to examine the out-of-plane components, as well. Since the petal interface locations were not shimmed in the z-direction, only the repeatability error (and not the accuracy error) is examined. Figure 21 shows the z-components of the repeatability error $\boldsymbol{D}_{ij}$ of the petal interface locations over all deployments, as well as the associated tolerance intervals (computed with, as before, $\gamma = 0.9973$, $(1-\alpha) = 0.90$, and $n = 22$). The out-of-plane deployment repeatability errors and the associated tolerance intervals fall within a ±244 µm band.

VI.H. Repeatability of Node Locations

Even though the measured node points are not directly relevant to Milestone 7C, it is useful to look at the repeatability of these points. This helps characterize the deployment repeatability of the entire truss. Since the node points are not shimmed, only their repeatability is reported. Figure 22 plots the radial and tangential components of the repeatability error of the measured node points, along with the size of the tolerance intervals. The in-plane components of the repeatability error at the nodes and the corresponding

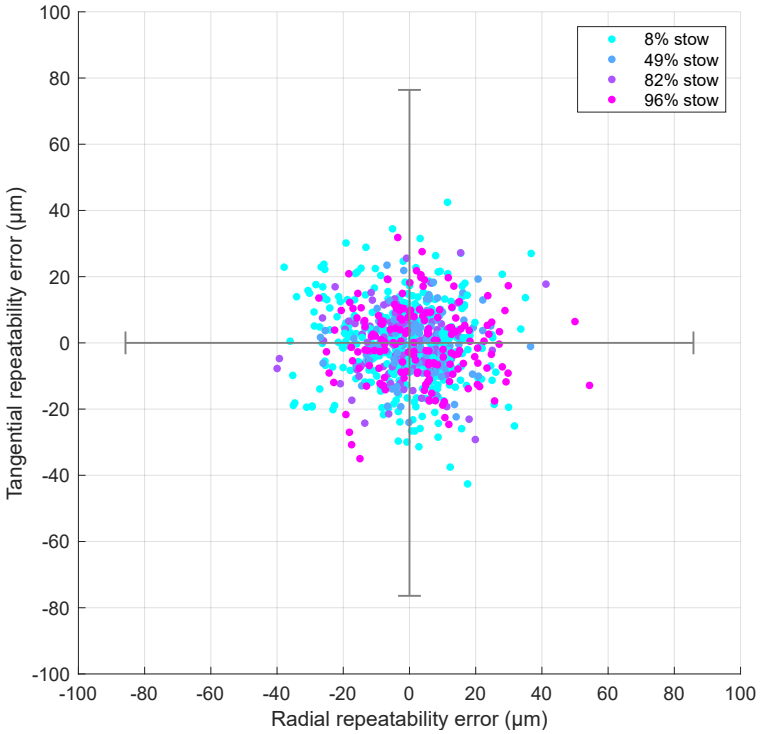

Figure 20: In-plane components of the deployment repeatability errors of the 34 measured petal interfaces over all 22 deployments. The bars represent the maximum radial and tangential tolerance intervals across the 34 petal interfaces. The color corresponds to the stow percent associated with the deployment. All deployment repeatability errors and the associated tolerance intervals fall within ±86 µm.

tolerance intervals falls within ±82 µm bands, which is comparable to the repeatability performance at the petal interfaces.

VI.I. Repeatability of Hub Location

Milestone 7C does not refer to the deployed petal interface positions with respect to the hub; however, it is instructive to examine how repeatably the petals are placed with respect to the hub. There are 3 SMRs on the hub that were measured. A 140 µm change in size of the triangle made by these 3 hub SMRS was observed over the 22 deployments. This is consistent with thermal expansion of the 2.2 m-diameter hub, constructed of aluminum (CTE of about 22 ppm°C^{-1}), over the measured air temperature range of 3.2 °C. The deployment repeatability of these three points will include a large contribution from this thermal expansion. To correct for this effect, the repeatability of the *centroid* of this triangle is evaluated. Table 5 lists the radial, tangential, and z tolerance intervals of this centroid. The radial and tangential basis vectors were evaluated based on the mean hub centroid position over all 22 deployments.

Radial tolerance interval	[±38 µm]
Tangential tolerance interval	[±60 µm]
Z tolerance interval	[±332 µm]

Table 5: Tolerance intervals associated with the repeatability error of the hub centroid.

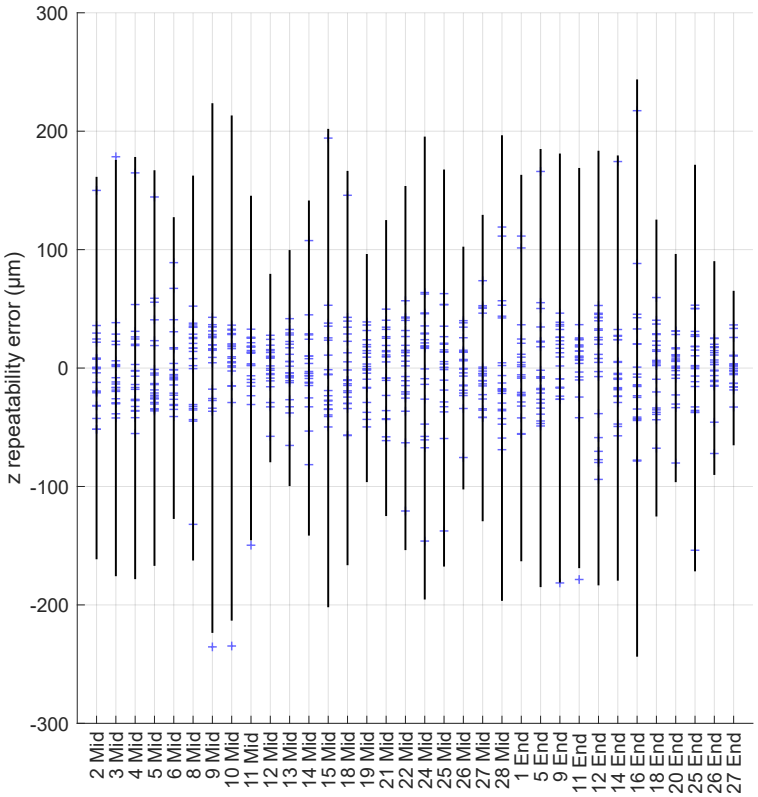

Figure 21: Out-of-plane components of the deployment repeatability errors of the 34 measured petal interfaces. The blue dashes represent repeatability errors from individual deployments, and the bars represent the tolerance intervals.

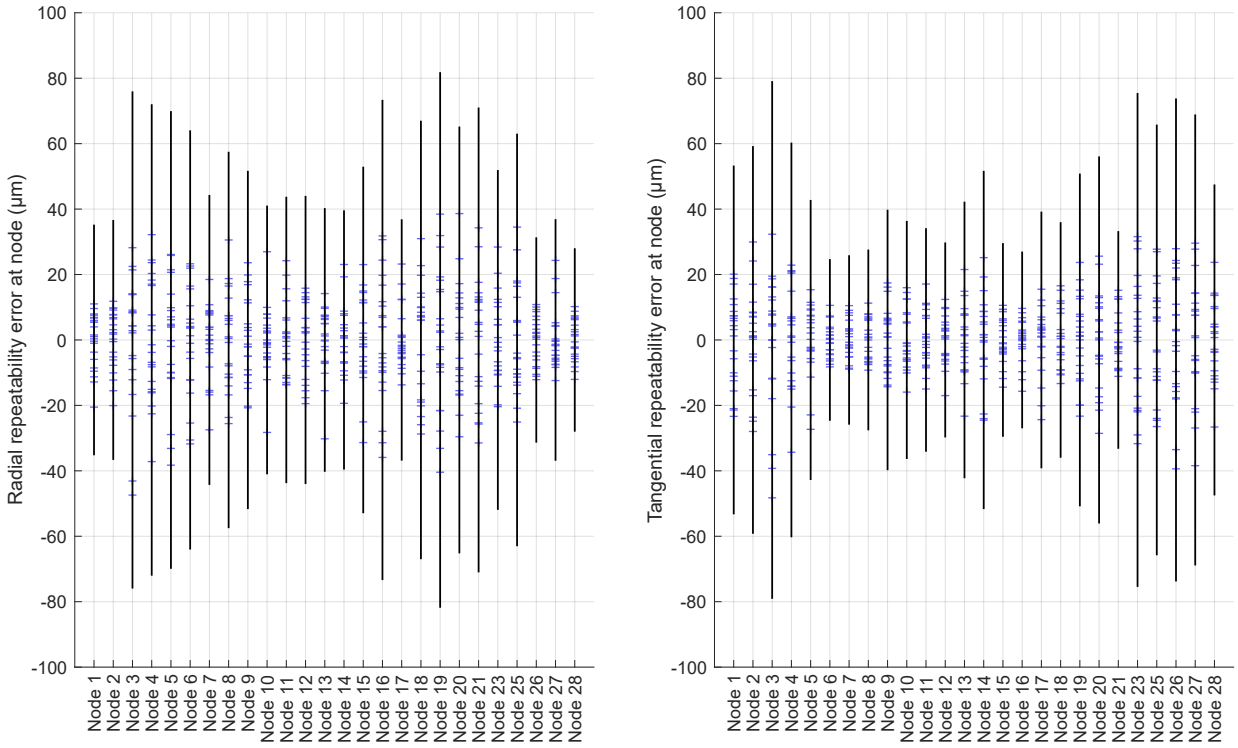

(a) Radial

(b) Tangential

Figure 22: In-plane components of the deployment repeatability errors of the perimeter truss nodes. The blue dashes represent repeatability errors from individual deployments and the bars represent the tolerance intervals. The numbering of the nodes is as per Figure 11.

VII. Discussion of Results

As can be seen in Figure 16, Figure 17, and Figure 19, the measured accuracy errors and the associated 3σ bounds fall within the required allocations. Table 6 lists the required allocations and the corresponding measured 3σ bounds. As can be seen, all error components have at least 19% margin. Based on this, we claim to have met Milestone 7C.

	Allocation	Measured 3σ bound	% margin
Radial bias	35 µm	26 µm	26
Radial random	150 µm	121 µm	19
Tangential random	120 µm	91 µm	24

Table 6: Required allocations for the petal position accuracy errors and the measured 3σ bounds.

As can be seen in Figure 16, the bounds on the radial and tangential random components are constrained primarily by 3 of the measured 34 petal interfaces. Examining Figure 17, these 3 petal interfaces can be identified as the middle petal interfaces on longerons 8, 9, and 21. These are the only petal interfaces with the radial and tangential components of the mean accuracy error greater than 50 µm. These petal interfaces represent the worst-shimmed of the 34 petal interface measured. Through better shimming, their mean accuracy errors could be reduced. Such improved shimming is clearly possible, given the performance of the other 31 of the petal interfaces.

Based on Figure 20, the in-plane deployment repeatability errors and the tolerance intervals are contained within ±86 µm. This represents the deployment accuracy achievable with perfect shimming. Better shimming can be achieved by conducting more rounds of deployment and measurement to reduce uncertainty in $\overline{\boldsymbol{p}}_i$, by using smaller increments of shim correction to "creep up" on the desired shim state, and by using multiple or more capable laser trackers to reduce measurement uncertainty.

This result is also relevant for the scaling up of the IDS to larger-diameter starshades, e.g. the 52 m-diameter HabEx starshade. While deployment repeatability errors can reasonably be expected to grow with the size of the IDS, shimming errors should not grow in a similar fashion.

VII.A. Validity of Partial Stows

Based on the measured data, the validity of the approach of using partial stows can be evaluated. This can be done by examining changes in the distribution of the repeatability errors as the stow percent is varied. The reason for examining repeatability errors as opposed to accuracy errors is that since the repeatability errors inherently have zero mean, all measured petal interface errors can be lumped into a single distribution; the accuracy errors for the petal interfaces have different means, and this collective examination would be impossible.

The in-plane repeatability errors of the petal interfaces plotted in Figure 20 are colored according to the associated stow percent; in this plot, the four different stow percents used (8%, 49%, 82%, and 96%) seem to exhibit similar spreads in deployment repeatability. For a clearer comparison, Figure 23 compares the distribution of these components in a histogram format. The histogram counts are normalized to account for the different number of deployments conducted from the different stow states; the area under each histogram is equal. For a numerical comparison, Table 7 lists the standard deviations of these populations.

Stow %	**Radial 1σ** (µm)	**Tangential 1σ** (µm)	**Number of points**
8	13.5	12.4	374
49	11.2	9.3	102
82	12.0	10.2	102
96	14.1	11.1	170

Table 7: Standard deviation of repeatability errors across all measured petal interfaces, by stow fraction.

It can be seen, based on Figure 23 and Table 7, there is little appreciable difference in the repeatability data between the four different stow percents used. This validates the use of partial deployments in this experiment.

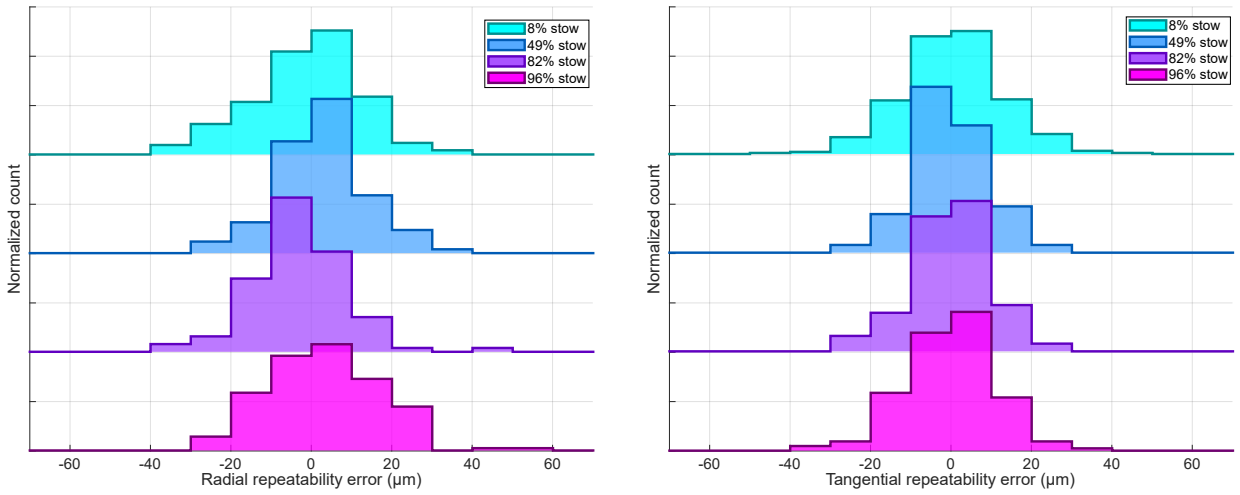

(a) (b)

Figure 23: Distribution of repeatability errors across all measured petal interfaces, broken down by stow fraction. Since different numbers of deployments were performed for each stow fraction, the histograms are normalized; the area under each plot is the same.

VII.B. Observed Deployment Anomalies

Over the 58 deployments conducted, two separate deployment anomalies were observed. In both these cases, the source of the anomaly was traced to incorrect stowage.

The first anomaly occurred on 16 July 2019 during the set of deployments conducted for shimming. One of the bottom-right spokes was stowed incorrectly, and during deployment it was caught behind an adjacent spoke interface at the hub. The deployment was halted and the IDS prototype was re-stowed. The stowage procedure was amended to include additional checks to ensure that the spokes were properly stowed, and this sort of anomaly did not reoccur.

The second anomaly occurred on 17 July 2019 during the set of 22 deployments conducted in the final shim state. The perimeter truss drive cable was stowed incorrectly such that it was caught under the ratchet at one of the diagonal assemblies on the perimeter truss. The drive cable remained caught in the deployed configuration. The stowage procedure was amended to check for the drive cable catches, and this sort of anomaly did not reoccur.

VII.C. Effects of Gravity and Gravity Compensation on Deployment Accuracy

The effects of gravity and gravity compensation forces must be considered; how does the deployment behavior of the IDS differ with Earth gravity and with discrete gravity compensation forces as compared to a zero-gravity environment? For brevity, the term "residual gravity forces" will be used to capture the combination of gravity and (possibly off-nominal) gravity compensation forces.

Two questions regarding the effects of residual gravity forces are significant:

1. To what degree do the residual gravity forces affect *the deployed shape* of the IDS?

2. To what degree do the residual gravity forces affect *the deployment repeatability* of the IDS?

An advantage of the orientation of the experimental setup is that the residual gravity forces act primarily in the out-of-plane direction, whereas the relevant shape tolerances are in-plane. Thus, residual gravity forces are unlikely to have first-order effects on the critical shape parameters.

The first question is straightforward to answer: a structural model of the IDS, described in Section VII.D, was used to estimate the deflections due to the residual gravity forces. Using a Monte Carlo approach, off-nominal gravity offload forces were applied, as well as forces due to gravity. The off-nominal gravity offload forces were computed using off-vertical offload angles normally distributed with $3\sigma = 0.29°$, which corresponds to a 25 mm position error of an offload cart at a 5 m height, and offload counterweight errors

normally distributed with $3\sigma = 1\%$; these represent conservative bounds for the experimental conditions. The resulting in-plane deflections were distributed with $3\sigma = 9\,\mu m$.

The answer to the second question is less straightforward. This answer must begin with a discussion of the physical mechanisms that give rise to imperfect deployment repeatability, i.e. the processes that produce different deployed shapes. Once these processes have been understood, the effect of residual gravity forces on these processes can be estimated. Listed below are possible mechanisms that lead to differences in deployed shape, as well as quantitative estimates of the degree of shape change caused by the most significant of these processes:

1. Dimensional change due to moisture absorption. CFRP, the primary perimeter truss and spoke material, absorbs water from the atmosphere and swells. Changes in the amount of water absorbed cause changes in size. The hygrothermal strain (i.e. the material strain due to water absorption) ϵ_H is linearly related to the amount of water absorbed, expressed as the mass percent of water ($\%m$), through the coefficient of moisture expansion (CME) β: $\epsilon_H = \beta(\%m)$. Carbon fiber/epoxy laminates have a CME of approximately 90×10^{-6} per % of water absorbed and a maximum water absorption capacity of approximately 0.90%.[19] Over the course of the final 22 deployments, the relative humidity was measured by the laser tracker weather station to be between 29% and 64%, which is a 34% variation. Assuming ($\%m$) also varies by 34% of its maximum value gives the variation in ($\%m$) as $\pm 0.153\%$. Thus the variation in the hygrothermal strain ϵ_H is $\pm 14 \times 10^{-6}$, and the resulting variation in perimeter truss radius is $\pm 74\,\mu m$.

2. Differences in distribution of prestress in the deployed structure will lead to changes in deployed shape. Based on the order in which the truss bays latch, the prestress distribution may be different after each deployment. Using the structural model described in Section VII.D and a Monte Carlo approach, the magnitude of shape errors due to variations in spoke preload were estimated to be $36\,\mu m$ at a 3σ level. This is based on a 3σ 1.2% variation of the spoke preload, which corresponds to a 3σ $50\,\mu m$ variation in deployed spoke length.

3. Variations in positions of the gravity compensation devices. This effect was analyzed above and found to produce shape variations of $9\,\mu m$ at the 3σ level.

4. Thermal strain of the IDS components can cause changes in deployed shape. The primary structural components of the truss – the longerons and the shorterons – have CTE of approximately $1 \times 10^{-6}\,°C^{-1}$. Based on the observed air temperature swings of $\pm 1.6\,°C$ over the many days of deployments, a shape change of as much as $\pm 8\,\mu m$ can be expected at the petal interfaces. Additionally, spatial differences in temperature of up to $0.8\,°C$ were observed in the deployed truss; these spatial differences were time-varying, depending on the time of day. Such spatial temperature variations cause non-uniform expansion and contraction, and would have contributed to IDS shape errors.

5. Creep, plasticity, damage, wear, or other inelastic effects. These effects would manifest as time-dependent trends in the measured deployment accuracy data. Over the 22 deployments, an overall increase in IDS radius of $14\,\mu m$ was observed, leading to shape errors in the range of $\pm 7\,\mu m$. Thermal and moisture expansion may explain some portion of this observation; however, it is expected that the greater part of this radius increase is due to inelastic effects. Progressive damage to the OS structure may have also contributed to this effect, through the compliant structural coupling between the perimeter truss and the OS. This effect warrants further investigation.

6. Variations in the relative arrangement of components (e.g. longerons, shorterons, nodes), due to "free-play" or mechanical slop between components being "taken up" in different ways upon deployment. Slop is necessary for the assembly of these components and for free motion in revolute joints. The deployed preload is intended to "take up" the slop in a predictable fashion; however, due to friction, imperfect geometries of components, and other effects, this may not happen. Based on bounding calculations, the maximum changes in deployed shape due to slop are $\pm 1\,\mu m$.

Table 8 summarizes these processes and the estimated magnitude of their effect on deployment repeatability. The RSS total of these effects is $\pm 83\,\mu m$, which agrees remarkably well with the measured $\pm 86\,\mu m$ deployment repeatability (see Section VII). Table 8 also rates the effect of residual gravity forces on these process on a scale of None, Low, Medium, and High.

Process	Magnitude (µm)	Effect of residual gravity forces
Moisture absorption	74	None
Prestress variation	36	Medium
Gravity offload	9	High
Thermal strain	8	None
Inelastic effects	7	Low
Free-play	1	Medium

Table 8: The processes that contribute variations in deployed shape, estimates of the size of the effect of these processes on deployment repeatability (expressed as 3σ or $\pm$ limits), and the degree to which residual gravity forces affect these processes.

The majority of the variations in deployed shape are likely due to processes unaffected by residual gravity forces. Additionally, residual gravity forces act primarily to *degrade* the deployment repeatability, making this experiment a conservative test as compared to a space-based deployment. That being said, it is also possible that the residual gravity forces *suppress*, for instance, the size of spoke prestress variations, and thus *improve* deployment repeatability on the ground as compared to in-space. Additional testing and analysis is necessary to completely capture the effects of residual gravity forces on deployment accuracy.

VII.D. Structural Model of the Deployed IDS

The stiffness of the deployed IDS can be captured by a prestressed pin-jointed truss model.[20–22] The stiffness matrix $\mathbf{K}$ relates the nodal displacements $\mathbf{d}$ to the applied nodal forces $\mathbf{f}$:

$$\mathbf{Kd} = \mathbf{f} \tag{17}$$

$$\mathbf{K} = \mathbf{AGA}^T - \mathbf{A}\hat{\mathbf{T}}\mathbf{A}^T + \mathbf{S} \tag{18}$$

where $(\mathbf{AGA}^T)$ represents the material stiffness of the members, and $(-\mathbf{A}\hat{\mathbf{T}}\mathbf{A}^T + \mathbf{S})$ represents the stiffness due to prestress. $\mathbf{A}$ is the equilibrium matrix, $\mathbf{G}$ is a diagonal matrix of bar axial stiffnesses EA/L, $\hat{\mathbf{T}}$ is a diagonal matrix of bar tension densities t/L, and $\mathbf{S}$ is the stress matrix. The exact definitions and methods for constructing these matrices can be found in.[22]

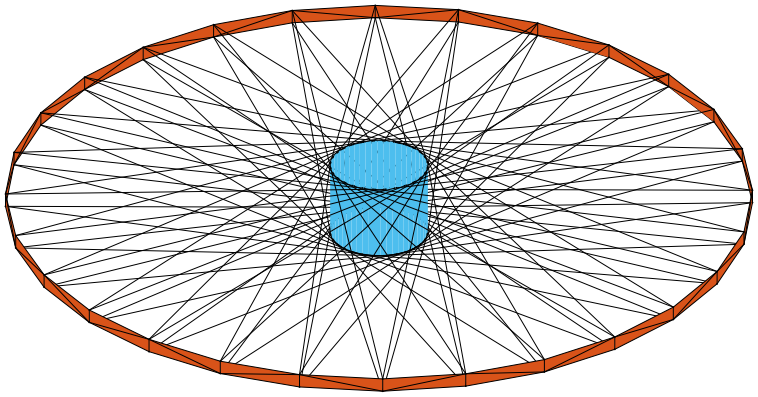

Figure 24: Structural model of the IDS.

The IDS prototype is not exactly a pin-jointed framework; however, the following simplifying assumptions makes the structure amenable to such analysis:

1. The truss node, which in reality is a stiff triangular structure, is represented by a single vertical bar.
2. The connections between the truss members – the longerons, the shorterons, the diagonals – and the truss nodes are assumed to be pin joints, incapable of transferring moments, whereas in reality these connections can transfer moments orthogonal to the axis of the revolute joint.

The structural model, illustrated in Figure 24, consists of 56 vertices at the truss, 2 for each of the 28 truss bays, and 112 vertices at the hub, 4 for every truss bay. The truss nodes, the truss longerons and shorterons, the truss diagonals, and the spokes are represented as axially loaded bars. The vertices at the hub are held constrained in all 3 translational degrees of freedom, and forces are applied to the vertices at the truss. In the prestressed state, spoke tension is 71 N, longeron compression is 626 N, node tension is 12 N, and the diagonal is unstressed. Table 9 lists the axial stiffnesses of the members used for this analysis.

	E (GPa)	A (mm^2)	EA (N)
Longeron	124	116	1.43×10^7
Node	69	293	2.03×10^7
Diagonal	124	59	7.30×10^6
Spoke			90.1×10^3

Table 9: Member axial stiffnesses used for the structural model.

VIII. Conclusions

This paper has demonstrated that the Inner Disk Subsystem (IDS) of the "wrapped" starshade mechanical architecture can deploy with the tolerances required for the SRM mission concept. The pertinent components of the shape accuracy errors of the petal interfaces were all measured to be below the required allocations at a 3σ level, with at least 19% margin. The measured deployment repeatability, which represents the ultimate accuracy capability of the IDS assuming perfect shimming, was measured to be $\pm 86\,\mu$m.

This is the first time a full-scale optical shield has been realized and integrated with the IDS. It was demonstrated that the required IDS deployment accuracy is achievable with an integrated optical shield.

Another key aspect of this demonstration is the design of the gravity compensation systems. It was demonstrated that it is possible to conduct tens of deployment tests in Earth gravity while compensating for gravity throughout. The ability to perform multiple relevant deployments on the ground will be key for the future development and maturation of this technology.

VIII.A. Future Work

In the short term, work is underway to build numerical models of the IDS deployment, and gather data from this testbed to validate these numerical models (e.g. position data throughout deployment, deployed stiffness, and force profiles throughout deployment).

In the longer term, the work presented here is a precursor for the tests that will be done to meet Milestone 7D of the S5 activity, which is listed here for reference:[4]

> Inner Disk Subsystem with optical shield assembly *that includes all features* demonstrates repeatable deployment accuracy consistent with a total pre-launch petal position accuracy within $\pm$ 300 µm.

The testbed for Milestone 7D will comprise medium-fidelity components (perimeter truss, spokes, optical shield) and also four 6 m-long petals attached to four truss bays. The remaining truss bays will be populated with "petal stubs" that capture the interface between the petal and the perimeter truss. This testbed will be required to demonstrate in-plane deployment accuracy to a $\pm 300\,\mu$m level, as well. Lessons learned from the present testbed will be applied to the design of the next generation of hardware.

Acknowledgments

Many thanks to the interns and engineers at JPL, Roccor, and Tendeg who assisted with the construction of the test hardware and the conduction of the experiments. The research was carried out at the Jet Propulsion Laboratory, California Institute of Technology, under a contract with the National Aeronautics and Space Administration (80NM0018D004).

References

[1]Cash, W., "Detection of Earth-like planets around nearby stars using a petal-shaped occulter," *Nature*, Vol. 442, No. 7098, 2006, pp. 51–53.

[2]Cash, W., Schindhelm, E., Arenberg, J., Polidan, R., Kilston, S., and Noecker, C., "The New Worlds Observer: using occulters to directly observe planets," *Proc. SPIE 6265, Space Telescopes and Instrumentation I: Optical, Infrared, and Millimeter*, Vol. 6265, June 2006, p. 62651V.

[3]Seager, S., Turnbull, M., Sparks, W., Thomson, M., Shaklan, S. B., Roberge, A., Kuchner, M., Kasdin, N. J., Domagal-Goldman, S., Cash, W., Warfield, K., Lisman, D., Scharf, D., Webb, D., Trabert, R., Martin, S., Cady, E., and Heneghan, C., "The Exo-S probe class starshade mission," *Proc. SPIE 9605, Techniques and Instrumentation for Detection of Exoplanets VII*, Vol. 9605, 2015.

[4]Willems, P., "Starshade to TRL5 (S5) Technology Development Plan," Tech. rep., Jet Propulsion Laboratory, Dec. 2018.

[5]Flinois, T., Bottom, M., Martin, S., Scharf, D., Davis, M. C., and Shaklan, S., "S5: Starshade technology to TRL5 Milestone 4 Final Report: Lateral formation sensing and control," Tech. rep., Nov. 2018.

[6]Harness, A., Kasdin, N. J., Galvin, M., Shaklan, S., Balasubramanian, K., White, V., Muller, R., Dumont, P., Vuong, S., and Willems, P., "Starshade Technology Development Activity Milestone 1A: Demonstration of High Contrast in Monochromatic Light at a Flight-like Fresnel Number," Tech. rep., June 2019.

[7]Harness, A., Kasdin, N. J., Galvin, M., Shaklan, S., Balasubramanian, K., White, V., Muller, R., Dumont, P., Vuong, S., and Willems, P., "Starshade Technology Development Activity Milestone 1B: Demonstration of High Contrast in Broadband Light at a Flight-like Fresnel Number," Tech. rep., March 2019.

[8]Kasdin, N. J., Spergel, D. N., Vanderbei, R., Shaklan, S., Lisman, D., Thomson, M., Marks, G., Lo, A., and Macintosh, B., "Verifying Deployment Tolerances of an External Occulter for Starlight Suppression," TDEM Report, 2014.

[9]Hirsch, B., Webb, D., and Thomson, M., "Starshade Deployable Inner Disk Structure Design and Development," *3rd AIAA Spacecraft Structures Conference*, San Diego, California, USA, Jan. 2016.

[10]Seager, S., Kasdin, N. J., et al., "Starshade Rendezvous Probe Study Report," Tech. rep., Feb. 2019.

[11]Gaudi, S., Seager, S., et al., "HabEx: Habitable Exoplanet Observatory Final Report," Tech. rep., Aug. 2019.

[12]Webb, D., Hirsch, B., Bach, V., Sauder, J., Bradford, S. C., and Thomson, M., "Starshade Mechanical Architecture & Technology Effort," *3rd AIAA Spacecraft Structures Conference*, San Diego, California, USA, Jan. 2016.

[13]Thomson, M., "The AstroMesh deployable reflector," *IEEE Antennas and Propagation Society International Symposium Digest*, Vol. 3, 1999, pp. 1516–1519.

[14]Zirbel, S. A., Lang, R. J., Thomson, M. W., Sigel, D. A., Walkemeyer, P. E., Trease, B. P., Magleby, S. P., and Howell, L. L., "Accommodating Thickness in Origami-Based Deployable Arrays," *Journal of Mechanical Design*, Vol. 135, No. 11, Oct. 2013, pp. 111005.

[15]Sigel, D., Trease, B. P., Thomson, M. W., Webb, D. R., Willis, P., and Lisman, P. D., "Application of Origami in Starshade Spacecraft Blanket Design," *Proceedings of the ASME 38th Mechanisms and Robotics Conference IDETC/CIE 2014*, Buffalo, New York, Aug. 2014.

[16]Leica Geosystems, "Leica AT402 User Manual," 2013.

[17]Leica Geosystems, "Leica Absolute Tracker AT401 White Paper," 2010.

[18]Jensen, W. A., "Approximations of Tolerance Intervals for Normally Distributed Data," *Quality and Reliability Engineering International*, Vol. 25, 2009, pp. 571–580.

[19]European Cooperation for Space Standardization, "Structural materials handbook - Part 1: Overivew and material properties and applications," *Space engineering*, 2011.

[20]Pellegrino, S., "Analysis of prestressed mechanisms," *International Journal of Solids and Structures*, Vol. 26, No. 12, 1990, pp. 1329–1350.

[21]Pellegrino, S., "Structural computations with the singular value decomposition of the equilibrium matrix," *International Journal of Solids and Structures*, Vol. 30, 1993, pp. 3025–3035.

[22]Guest, S., "The stiffness of prestressed frameworks: A unifying approach," *International Journal of Solids and Structures*, Vol. 43, 2006, pp. 842–854.